

DENOISING: FROM CLASSICAL METHODS TO DEEP CNNs

JEAN-ERIC CAMPAGNE

Université Paris-Saclay, CNRS/IN2P3, IJCLab, 91405 Orsay, France

ABSTRACT. This paper aims to explore the evolution of image denoising in a pedagogical way. We briefly review classical methods such as Fourier analysis and wavelet bases, highlighting the challenges they faced until the emergence of neural networks, notably the U-Net, in the 2010s. The remarkable performance of these networks has been demonstrated in studies such as Kadkhodaie et al. (2024). They exhibit adaptability to various image types, including those with fixed regularity, facial images, and bedroom scenes, achieving optimal results and biased towards geometry-adaptive harmonic basis. The introduction of score diffusion has played a crucial role in image generation. In this context, denoising becomes essential as it facilitates the estimation of probability density scores. We discuss the prerequisites for genuine learning of probability densities, offering insights that extend from mathematical research to the implications of universal structures.

Keywords. denoising, Fourier analysis, wavelet analysis, diffusion models, U-Net

1. INTRODUCTION

Noise reduction is a crucial step in signal processing, aiming to restore a signal of interest disturbed by unwanted interferences. Noise perception is often subjective, as what constitutes a relevant signal for some may be considered noise for others, and vice versa. Thus, the primary objective of noise reduction is to recover the useful signal while minimizing the impact of stochastic disturbances. Recent advancements in generative models, particularly those based on score matching (Song et al., 2021), have sparked renewed interest in noise reduction, opening new perspectives in this field.

In this pedagogical article, while it's impossible to cover all aspects of noise reduction, we focus on a noise reduction method that exploits deep neural networks to reveal what the network learns. For comprehensive reviews, one can refer, for example, to Kong et al. (2023); Rama Lakshmi et al. (2023); Wang et al. (2020). However, to contextualize these advancements, we also examine traditional noise reduction approaches based on classic orthonormal bases. We highlight the differences between Fourier transform-based and wavelet-based analysis, as well as the limitations of each approach. Furthermore, we explore in detail how deep neural networks, such as DnCNN (Zhang et al., 2017) and U-Net (Ronneberger et al., 2015), push the boundaries of traditional methods. We will see how they achieve this and what they learn. To support our claims, we rely on previous works, notably that of Kadkhodaie et al. (2024).

For the sake of brevity, we limit our study to the case of additive white Gaussian noise, leaving aside issues related to observation acquisition.

2. NOISE REDUCTION IN "CLASSICAL" ORTHONORMAL BASES

To illustrate, let $x(u)$ denote an original signal with real values, where u is the low-dimensional variable indexing the sample: for example, $u = i$ could be a "time" index in the case of an audio frame, or $u = (i, j)$ a double index to locate a pixel in an image. We assume that $x(u)$ is not affected

E-mail address: jean-eric.campagne@ijclab.in2p3.fr.

Date: April 26, 2024.

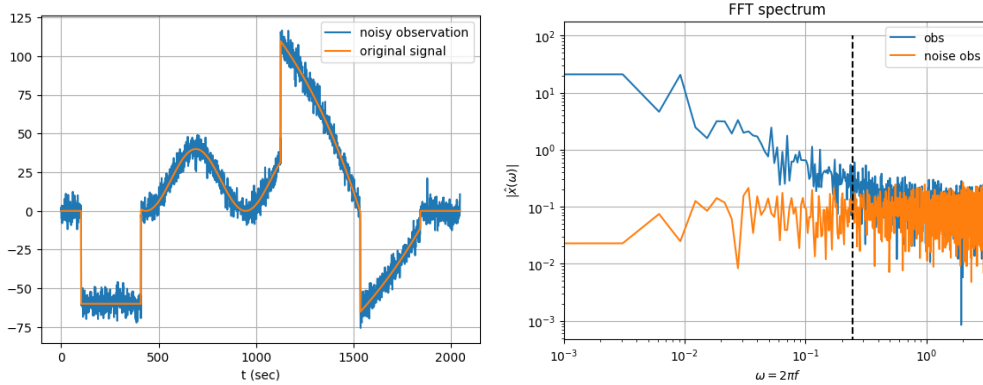


FIGURE 1. Left: Unnoised signal and its noisy observation ($\sigma = 5$). Right: Power spectra of the noisy signal and of the noise alone (re-synthesized).

by quantization effects. To this signal, we add noise $z(u)$, which we consider to be uncorrelated Gaussian white noise with variance σ^2 , so the observations $y(u)$ can be written as

$$(1) \quad y(u) = x(u) + z(u) \quad z \sim \mathcal{N}(0, \sigma^2)$$

The task of a denoiser is to restore the original signal x from the observations y . Even if σ is *a priori* unknown, we will see how to obtain an estimate with the data. To simplify, in many cases, we assume that this estimation is sufficiently relevant.

To begin, let's consider the 1D case depicted in Figure 1, where the original signal and observations $\{y(i)\}_{i \leq N}$ ($N = 2028$ with $\Delta t = 1$ sec.) are superimposed. This type of signal is chosen to represent transient phenomena. Indeed, the vast majority of signals (music pieces, speeches, photos of landscapes, indoor scenes, or faces) are structured and exhibit transitions between regular intervals.

2.1. Fourier Analysis. A first idea that naturally arises is to consider the Fourier spectra of such signals, as presented in Figure 1 for those of the noisy signal $|\hat{y}(\omega)|$ ($\omega = 2\pi f$) and of the noise alone $|\hat{z}(\omega)|$ obtained by synthesizing the noise from an estimate of the variance obtained through preprocessing¹. Note that with $\Delta t = 1$ sec, the maximum accessible frequency is 0.5 Hz, or $\omega_{max} = \pi$, according to the Nyquist theorem. We observe that the spectral power of the noise approximately dominates for frequencies beyond $f_{cut} = 40$ mHz or $\omega_{cut} = 0.245$. If we depict the decomposition on the orthonormal Fourier basis as

$$(2) \quad y(k) = \sum_{\omega=0}^{\omega_{max}} \hat{y}(\omega) e^{i\omega k}$$

then we can establish a "Hard" thresholding strategy on the Fourier coefficients as follows:

$$(3) \quad \rho_{\omega_{cut}}(\hat{y}, \omega) = \begin{cases} \hat{y}(\omega) & \omega \leq \omega_{cut} \\ 0 & \omega > \omega_{cut} \end{cases}$$

which allows obtaining the low-frequency estimation of the original signal by performing the following summation:

$$(4) \quad \tilde{x}(k) = \sum_{\omega} \rho_{\omega_{cut}}(\hat{y}, \omega) e^{i\omega k} = \sum_{\omega < \omega_{cut}} \hat{y}(\omega) e^{i\omega k}$$

¹We will see later for the wavelet coefficient thresholding. In the case of the 1D signal, by taking the constant frame from the beginning, we use $\sigma = 1.4826 \times \text{MAD}(y(u) - \text{med}(y(u)))$ where MAD is the *Median Absolute Deviation*. One can also use an iterative method that allows determining an initial estimation of $x(u)$, which is subtracted from $y(u)$ to apply the same formula.

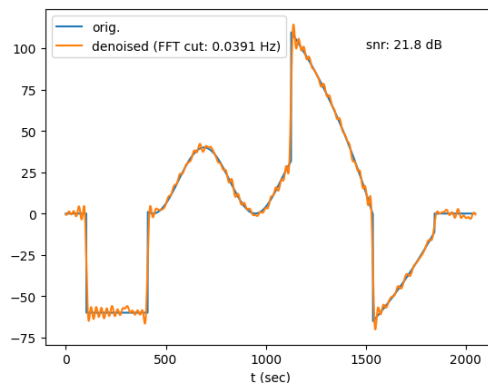


FIGURE 2. Original signal and its denoised version by a cutoff in the power spectrum.

The result of the thresholding in Eq. 3 is shown in Figure 2. Note in passing that this frequency thresholding mechanically translates, so to speak, into a thresholding on the Fourier coefficients. This is inherent to the nature of the Fourier transform; we will see the difference with wavelet analysis.

What do we observe? Firstly, we have indeed reduced the noise when compared to Figure 1, but upon closer inspection, there are artifacts in the form of small oscillations present everywhere, with more pronounced trends at the transition levels. This is where we perceive the flaws and limitations of the Fourier analysis approach. To begin with, let's recall a result concerning the relationship between the decay of the Fourier spectrum and the regularity of a function:

Theorem 1. *If g (1D) is bounded and there exist K and $\varepsilon > 0$ such that*

$$(5) \quad |\hat{g}(\omega)| \leq \frac{K}{1 + |\omega|^{n+1+\varepsilon}}$$

then $g \in C^n$, meaning that g is continuously differentiable n times.

This has three consequences: (1) we can "read" from the power spectrum the degree of regularity of the function, and the faster the decay, the more regular the function, (2) a function whose power spectrum has compact support ("bounded") is infinitely differentiable, (3) the decay of $|\hat{g}(\omega)|$ is governed by the worst regularity of the function over its entire domain. This latter property helps us understand the shape of the power spectrum of the observed signal (Fig. 1): since there are discontinuities, the spectrum is constrained to decay only as $1/|\omega|$, which is the shape of the Fourier spectrum of a "step-function." This constraint masks the fact that the function is regular outside the transition phases².

Therefore, as the observed spectrum decays slowly, when placing a cutoff to reduce white noise whose spectrum is constant, ω_{cut} (f_{cut}) must be relatively low frequency, depriving us of components resulting from transients. Moreover, by truncating the Fourier series, the residue is an oscillating function composed of high-frequency contributions, hence the oscillations. This phenomenon, which occurs due to thresholding, regardless of whether there is noise or not, is what we call the Gibbs phenomenon.

Now, one might consider that the employed thresholding is very abrupt, and we can gain insight into what happens by taking a filtering perspective. Indeed, let h be a real filter with spectral

²Note a technical point: notice that the chosen signal returns to the same level (0) at the beginning and end of the frame. If this were not the case, due to a simple FFT considering the periodic spectrum with a period equal to its length, we would then have a discontinuity that would generate a spectrum in $1/|\omega|$. To overcome this technical defect, one would need to use a Discrete Cosine Transform (DCT) that symmetrizes the signal by making it even before considering it periodic (this time with a period twice its length).

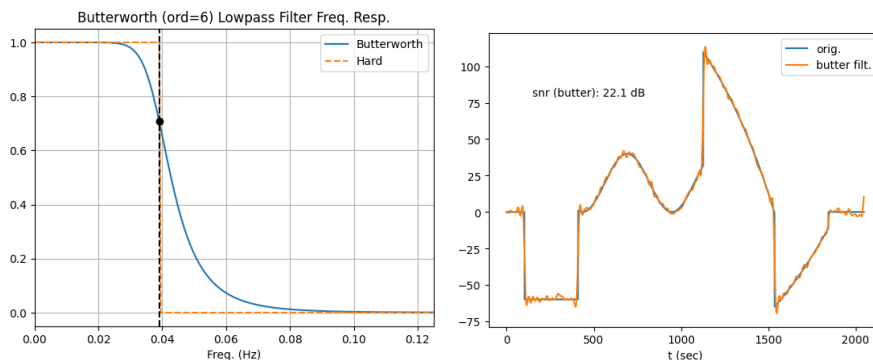


FIGURE 3. Left: Compared spectral responses of the Butterworth filter (order 6) and the square function. Right: Denoising of the signal Fig. 1 by the Butterworth filter (to compare with Figure 2).

response $\hat{h}(\omega)$; its usage proceeds with the following operations:

$$(6) \quad \hat{x}(\omega) = \hat{y}(\omega)\hat{h}(\omega) \Leftrightarrow \tilde{x}(k) = \sum_{\omega} \hat{y}(\omega)\hat{h}(\omega)e^{i\omega k} = \sum_{\omega} \rho_h(\hat{y}, \omega)e^{i\omega k}$$

where ρ defines a function generalizing the operation 3 by defining the associated filter as that of a square function used by Cl. Shannon. However, the operation of multiplying spectral responses in Eq. 6 translates to a convolution in the real domain:

$$(7) \quad \tilde{x}(k) = (y * h)(k) = (h * y)(k) = \int h(k - u)y(u)du$$

However, in the case of the square function, its counterpart in the real domain is the *sinc* function (i.e., the function $\sin(x)/x$), which is notoriously oscillatory and has long tails. We understand the effects of signal averaging that impairs signal reconstruction, especially in transition zones.

However, one could consider changing the filter h (or a function ρ_h) with a smoother spectral response beyond the cutoff frequency while still aiming to reduce the noise portion. There are many filters in the literature as they are widely used in electronics, notably Stephen Butterworth's eponymous filter (1930). Figure 3 presents the spectral response of this type of filter and its denoising action.

We observe that the result is slightly improved compared to Figure 2, but it is clear that the improvement is marginal. Certainly, other types of thresholding can be applied (Mallat, 2008), but the result is generally the same: we would need a tool that can analyze the function locally and concentrate the description into a sparse representation where the largest coefficients reveal the transients. One might consider performing what is called a windowed Fourier transform, but the major drawback lies in defining these windows. In fact, the tool should adapt automatically to the studied function. This tool has existed since the 1990s: it is the wavelet multi-resolution analysis discussed in the following section. The concepts developed for Fourier analysis prove useful in designing such analyses.

2.2. Wavelet Analysis.

2.2.1. *Some Basic Notions.* Wavelet theory is elaborated in detail in the reference book by Mallat (2008). Here are some elements within the scope of this article. A *wavelet* $\psi(x)$ is an oscillating function such that

$$(8) \quad \int_{-\infty}^{\infty} \psi(x) dx = 0$$

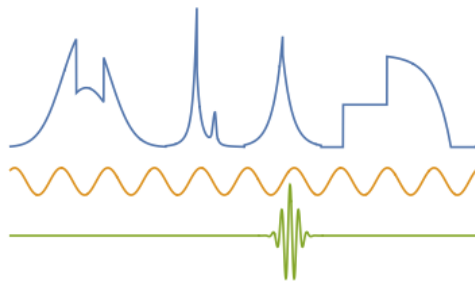


FIGURE 4. Difference between a sine wave and a wavelet in real space. The concentration of the wavelet allows non-zero coefficients $W_{j,n}(f)$ only around the discontinuities of the signal.

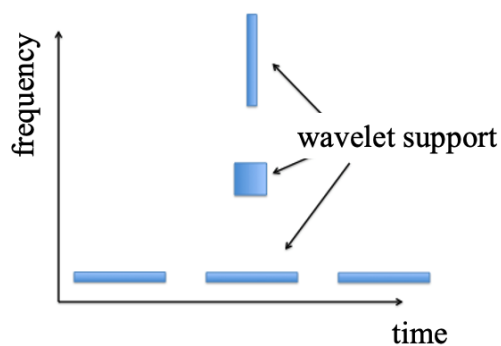


FIGURE 5. Schematic evolution of the wavelet support in the "time-frequency" plane.

thus, in the Fourier domain, it is a band-pass filter. This function undergoes translations and dyadic dilations/contractions³ such that, up to a normalization factor:

$$(9) \quad \psi_{n,j}(x) \propto \psi(2^j x - n), \quad j, n \in \mathbb{Z}$$

As j increases, the "size" of the support of the wavelet $\psi_{n,j}(x)$ contracts, and vice versa for $j < 0$. This allows for a local analysis of a function $f(x)$ by considering the inner products:

$$(10) \quad W_{j,n}(f) = \langle \psi_{n,j}, f \rangle = \int_{-\infty}^{\infty} f(v) \psi_{n,j}^*(v) dv$$

If the variations of f are slow compared to the support of $\psi_{n,j}(x)$, then $W_{j,n}(f)$ is zero. The difference between a sine wave and a wavelet for the analysis of signals with transients is clearly seen (Fig. 4): the wavelet provides a local introspection of the function unlike the sine wave.

In the Fourier domain, when considering dilations/contractions, we have the opposite effect compared to that in the real space:

$$(11) \quad \hat{\psi}_{n,j}(\omega) = \frac{1}{2^j} \hat{\psi}\left(\frac{\omega}{2^j}\right)$$

so for $j > 0$, the spectrum $\psi_{n,j}$ shifts towards high frequencies, while for $j < 0$, it is the opposite. Unlike a sine wave at a fixed frequency, which is delocalized in real space, a wavelet is localized in both spaces: the wavelet's support in the "time-frequency" plane is low-frequency and well-localized in frequency and quite wide in time, and conversely, at high frequency, the localization in time is good and less so in frequency. The total "area" of the support in the time-frequency plane satisfies the Heisenberg inequality (Fig. 5).

³In the case of audio signal processing, the base scale factor is rather $2^{1/Q}$ where Q acts like the notion of an octave.

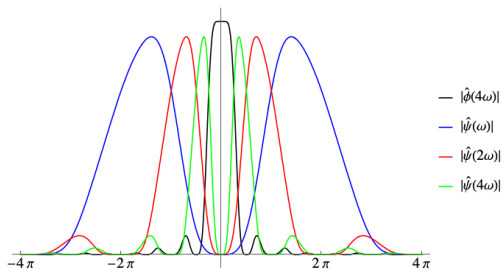


FIGURE 6. Coverage of the Fourier domain without gap by a low-pass filter and a collection of band-pass filters.

To determine whether $W_{j,n}(f)$ is significant or not, one can reason in the Fourier domain: slow variations of f imply that its spectrum is concentrated at low frequencies, and small scales of $\psi_{n,j}$ imply that the support of its Fourier spectrum is rather concentrated at high frequencies, so there is no overlap, hence the result $W_{j,n}(f) \approx 0$. On the contrary, where there are rapid variations of f during a transient, non-zero coefficients $W_{j,n}(f)$ can be found. Through the translations at a fixed scale j , the number of significant coefficients is typically given by the width of the wavelet. Hence the sought-after sparse representation at small scales that detect transients.

In fact, instead of considering the wavelets $\psi_{n,j}(x)$ with $j \leq 0$, to cover the entire Fourier domain allowing for a complete representation of a function f (Littlewood-Paley condition)⁴, one can use a low-pass filter denoted $\hat{\phi}(\omega)$. We only subject $\phi(x)$ to the translation operation, to obtain inner products:

$$(12) \quad V_n(f) = \langle \phi_n, f \rangle$$

An example of the complete collection of filters is given in Figure 6.

By inverse transformation, the coefficients $V_n(f)$ provide a large-scale approximation (low frequency) of f , while the coefficients $W_{j,n}(f)$ provide detailed information about the function. Thus, the complete characterization of a function f is done through the set of scalar products:

$$(13) \quad C(f) = \{V_n(f), W_{j,n}(f)\}_{j \in \mathbb{N}, n \in \mathbb{Z}}$$

In the specific case of multi-resolution analyses developed by S. Mallat, there is a relationship between $\hat{\phi}$ and $\hat{\psi}$, allowing the design of families of orthonormal bases of $L^2(\mathbb{R})$ (the space of square-integrable functions)⁵. Thus, I. Daubechies (1992) developed wavelets with *compact support* noted "db<n>". Figure 7 shows an example of ϕ and ψ ("db2"). The design of these wavelets is presented in Mallat (2008). The small spikes of the "db2" functions are not artifacts. The higher the n order of the wavelet, the more regular it is, as shown by the following theorem:

Theorem 2. (*Daubechies*)

If ψ has p zero moments⁶, then its support is at least equal to $2p - 1$, and the wavelets of type "db<p>" have a minimum support of $[-p + 1, p]$, and the corresponding support of ϕ is $[0, 2p - 1]$.

⁴Note: In the Fourier section, we saw that $\omega_{max} = \pi$ when considering a sampling frequency of 1, so the support of $\hat{\psi}(\omega)$ must cover this high part of the spectrum.

⁵The first orthonormal basis of $L^2(\mathbb{R})$ is that of A. Haar (1909), which is part of the Daubechies wavelet family "db1". D. Gabor and J. Morlet designed in 1948 and 1984 (following the "sniffer planes" affair) what would later be recognized as complex wavelets for their respective research, the first orthonormal basis of $L^2(\mathbb{R})$ and C^∞ being that of Y. Meyer (1986), thus initiating multi-resolution analysis and the development of fast transformation algorithms, including the work of S. Mallat (1989).

⁶The moment of order k is the result of $\int x^k \psi(x) dx$.

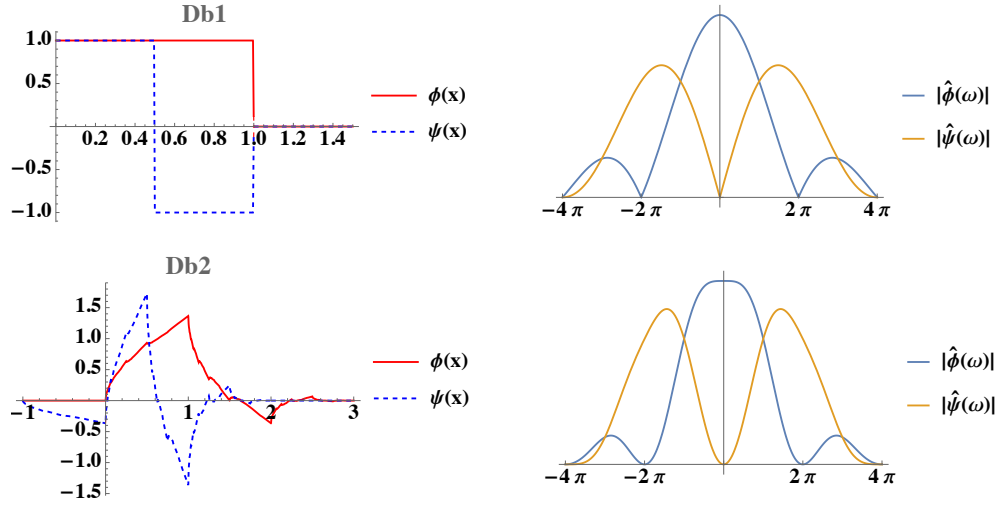


FIGURE 7. Daubechies wavelets of order 2 ("db1" or Haar at the top, "db2" at the bottom): left in the real space, right in Fourier space. ϕ is the low-pass filter, and ψ is the band-pass filter that provides the signal details.

If ϕ is also constrained to have zero moments, then we obtain Daubechies wavelets called "Coiflets"⁷. Other versions exist in libraries as PyWavelet (Lee et al., 2019) and Mathematical (Wolfram Research, Inc., 2022).

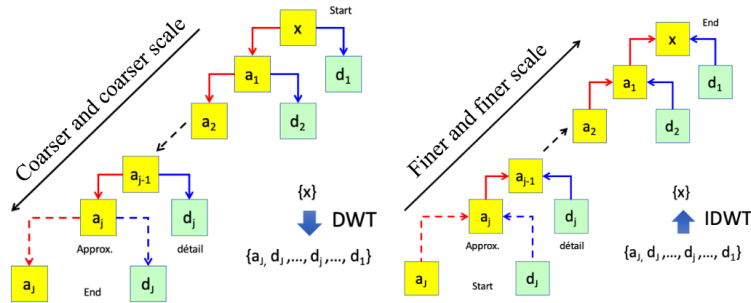


FIGURE 8. Illustration of the iterative wavelet transform (left) and the inverse transform (right).

These wavelets with compact support are very practical and allow the implementation of a fast wavelet transformation algorithm for a finite-size signal (and the inverse reconstruction) in $O(N)$ time, therefore faster than the FFT. Starting from the N samples of the signal, during a transformation, we obtain N coefficients⁸ where half of them constitute the low-frequency approximation coefficients, and the other half contains the detail coefficients (high-frequency). The process can then be iterated where at each step, the signal is replaced by the low-frequency coefficients from the previous step. For example, in three steps, an introspection of a signal is performed with filters $\{\hat{\phi}(2^j\omega), \hat{\psi}(2^j\omega)\}$ with $j = 0, 1, 2$ where only the wavelet coefficients obtained with the lowest

⁷The name is a tribute to R. Coiffman who asked I. Daubechies to find wavelets for quadratures.

⁸nb. except for adaptations at the edges

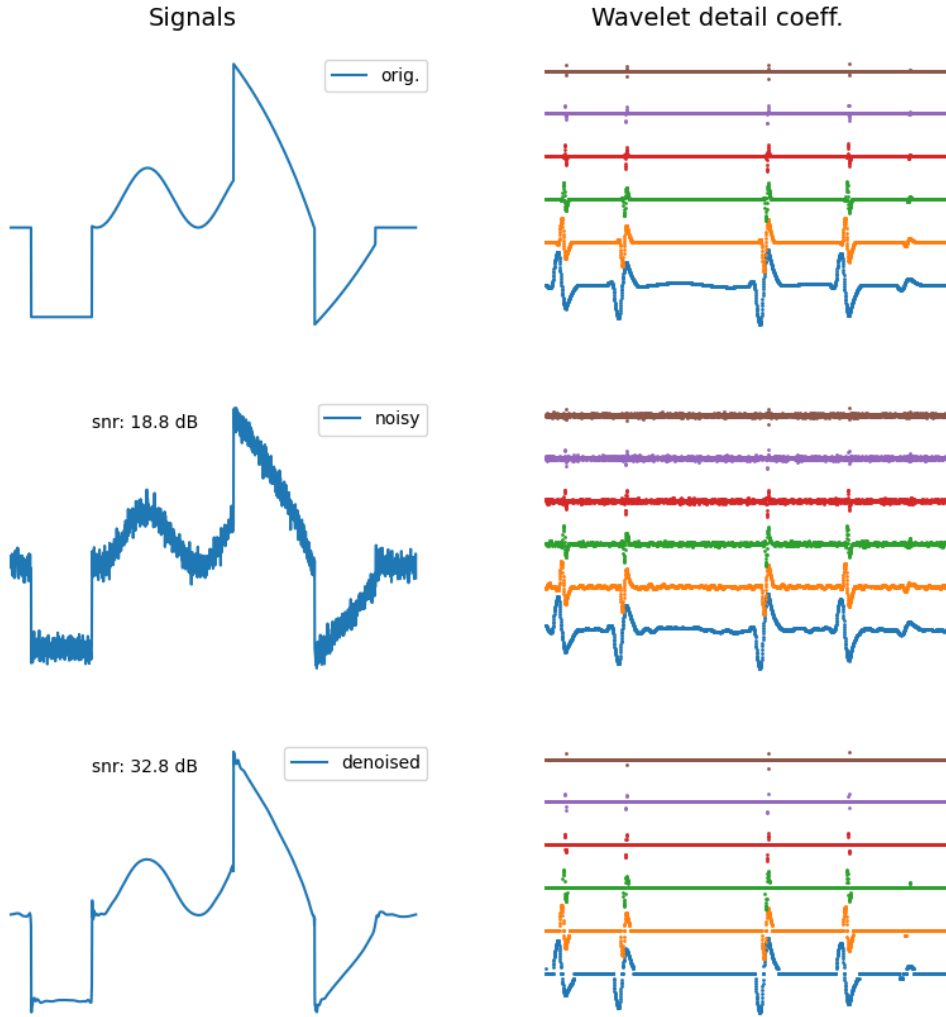


FIGURE 9. Denoising using thresholding of the detail coefficients from the wavelet decomposition of the observed signal.

frequency filter $\hat{\phi}(4\omega)$ and all detail filters $\hat{\psi}(2^j\omega)$ are retained, as shown in Figure 6. The schematization of these wavelet transformation steps (DWT for Discrete Wavelet Transform) and its inverse is given in Figure 8.

2.2.2. Application to 1D Denoising. On the right part of Figure 9 at the top, next to the graph of the noiseless signal x (Fig. 1), the coefficients $W_{j,n}(x)$ (the "details") concerning the largest scale at the bottom and the smallest scale at the top obtained by a fast wavelet transformation⁹ using the "db2" wavelets are shown. It can be observed that the significant coefficients are few (sparse) and concentrate as expected around the discontinuities of the signal.

Since the wavelet transformation is linear, the coefficients of the observed (noisy) signal y decompose as the sum of the coefficients of the noiseless (original) signal and the coefficients of the noise:

$$(14) \quad W_{j,n}(y) = W_{j,n}(x) + W_{j,n}(z)$$

⁹nb. In fact, a "stationary" or "translation-invariant" version of the transformation was used ("undecimated wavelet transform" or "à trous algorithm").

However, since the noise z comes from a random process (Gaussian white noise), the same applies to the coefficients $W_{j,n}(z)$. The "noisy" nature of $W_{j,n}(y)$ is observed in the middle part of Figure 9 on the right. However, it is also noticeable that the significant coefficients of the noiseless signal are hardly affected. One may then consider thresholding of the coefficients defined by¹⁰

$$(15) \quad \rho_T(W) = \begin{cases} 1 & |W| \geq T \\ 0 & |W| < T \end{cases}$$

If we denote by e_ℓ the elements of the orthonormal wavelet basis and $C_\ell(f)$ the wavelet coefficients of a function f (nb. ℓ is an index combining the pairs (j, n) from the representation Eq. 13):

$$(16) \quad f = \sum_{\ell} C_\ell(f) e_\ell$$

then the estimation of the signal x from the observed signal y is performed as follows:

$$(17) \quad \tilde{x} = \sum_{\ell} \rho_T(C_\ell(y)) e_\ell$$

Notice the similarity to expression 4 used in the context of Fourier analysis. However, there is a major difference, as the sum above can be written in the form:

$$(18) \quad \tilde{x} = \sum_{\ell \in \mathcal{E}_T} C_\ell(y) e_\ell$$

with

$$(19) \quad \mathcal{E}_T = \{\ell \text{ such that } |C_\ell(y)| \geq T\}$$

The difference lies in the fact that the membership condition to \mathcal{E}_T is conditioned by $C_\ell(y)$, which depends on the (observed) signal y , it is not the form $\ell < \ell_{cut}$ of equation 3 used in the Fourier framework. The condition adapts automatically to the shape of y , notably to its transient phases. This is what was sought with sparsity to overcome the shortcomings identified by Fourier analysis.

The choice to clarify is that of the threshold T . It is owed to D. L. Donoho and I. M. Johnstone (1990s) (Theorem 4 Sec. 3.4) who found that for a large class of problems

$$(20) \quad T = \sigma \times \sqrt{2 \log N} \quad (\text{Donoho \& Johnstone})$$

achieves nearly optimal risk¹¹ and moreover, the wavelet coefficients of the noise are such that

$$(21) \quad \lim_{N \rightarrow \infty} \mathbb{P} \left(T - \frac{\sigma \log \log N}{\log N} \leq \max_{0 \leq \ell < N} |C_\ell(z)| \leq T \right) = 1$$

The fact that T increases with N reflects the statistics of Gaussian white noise, which makes more and more excursions into the tails of the Gaussian as N increases. Moreover, the value of σ can be obtained by using the Median Absolute Deviation calculated on the detail coefficients of the highest frequency (smallest scale) and adjusted by a coefficient that links it to the variance of a Gaussian¹².

The result of such thresholding for the case of the noisy signal is shown in Figure 9 (bottom left plot). A noticeable improvement can be observed compared to Figure 2 obtained by Fourier analysis. To provide a quantitative expression for this visual impression, I have reported the signal-to-noise ratio (SNR¹³). In this case, if the noisy signal has an SNR of approximately 19 dB, the signal denoised by Fourier analysis achieves an SNR of 22 dB, while by wavelet analysis, an SNR of 39 dB is achieved. Therefore, wavelet analysis presents significant advantages over Fourier analysis in the case of signals containing transients. Let's see how this applies to images.

¹⁰nb. This is a "hard" thresholding in the literature and libraries.

¹¹Indeed, one can find a slightly smaller value that performs better.

¹²The coefficient is equal to 1.4826, it is the inverse of the quantile of the $\mathbb{N}(0, 1)$ distribution equal to 3/4.

¹³nb. its definition is $\text{snr}(x, x_{ref}) = 10 \log_{10} \left(\frac{\|x_{ref}\|^2}{\|x_{ref} - x\|^2} \right)$ with x_{ref} being the noise-free signal

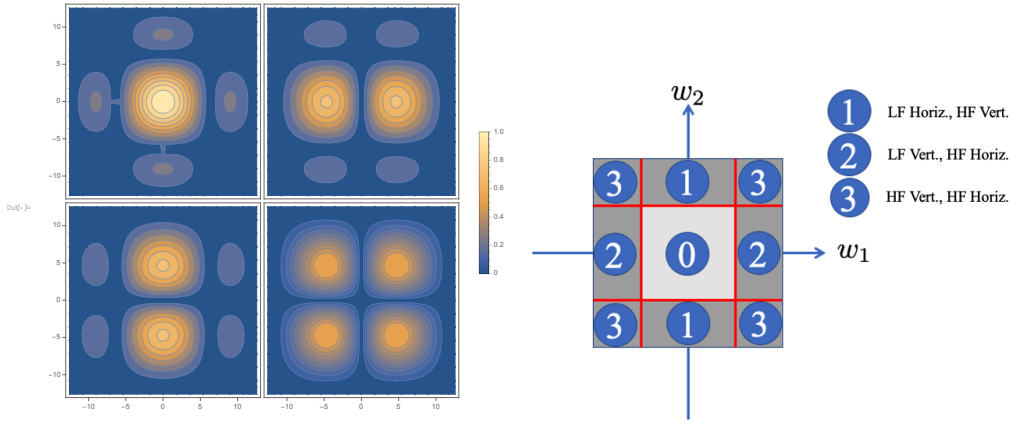


FIGURE 10. On the left: Coverage of the Fourier plane by different types of 2D wavelets constructed from 1D wavelets. On the right: corresponding diagram with the low-pass filter ("0") and various band-pass filters detecting details on rapid (transient) variations in three different directions (HF: high frequency, LF: Low frequency, Horiz.: horizontal, Vert.: vertical). The base wavelet is the Haar wavelet ("db1").

2.2.3. *Application to 2D denoising.* The wavelet theory described briefly in the previous section for the 1D case adapts quite easily to the multi-dimensional case (Mallat, 2008). Essentially, one needs to have a low-pass filter and a series of band-pass filters that together cover the necessary Fourier domain to decompose a function on an orthonormal basis.

In the 2D case, one can construct a representation from the 1D described functions ϕ and ψ , defining 3 wavelets that cover 3 Fourier zones as follows:

$$(22) \quad \begin{cases} \psi^1(u_1, u_2) &= \psi(u_1)\phi(u_2) \\ \psi^2(u_1, u_2) &= \phi(u_1)\psi(u_2) \\ \psi^3(u_1, u_2) &= \psi(u_1)\psi(u_2) \end{cases}$$

As this needs to be done at all scales, these three wavelets are dilated/contracted and translated according to

$$(23) \quad \psi_{j,n}^k(u) = \frac{1}{2^j} \psi^k\left(\frac{u - 2^j n}{2^j}\right) \quad u = (u_1, u_2), \quad n = (n_1, n_2)$$

The three types of wavelets detect *horizontal* contours, i.e., rapidly varying along the vertical axis hence vertical high frequencies, *vertical* contours, i.e., rapidly varying along the horizontal axis hence horizontal high frequencies, and finally contours that involve both types of variations. The low-pass filter

$$(24) \quad \phi(u_1, u_2) = \phi(u_1)\phi(u_2)$$

allows obtaining an averaged approximation. It just needs to be translated following the same principle as for the 1D case to cover the support of the function to be processed. An example is given with the Haar wavelets ("db1") in Figure 10.

The same type of progressive decomposition of an image into low-frequency approximation and detail coefficients is identical to the case described in the section dealing with 1D, using Daubechies wavelets, for example. An example illustrating this is shown in Figure 11. The detection of contours marking transients, as in 1D, can be observed. The gray areas indicate nearly zero coefficients, while significant amplitude coefficients are represented by white or black pixels depending on their sign. As observed, we indeed have a sparse representation. Now, as in 1D, progressively, the low-frequency approximation at step j of size $N_j \times N_j$ is decomposed into 4 sub-images of sizes $N_j/2 \times N_j/2$ with a

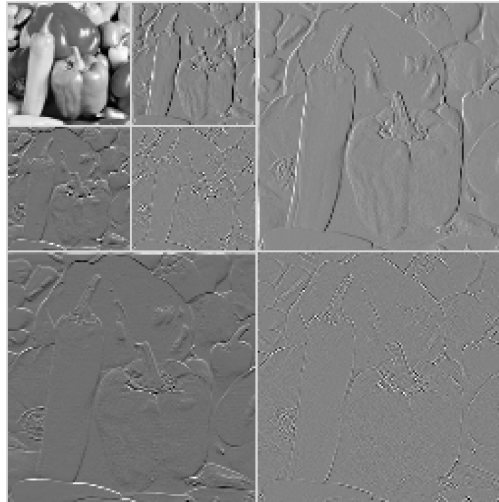


FIGURE 11. Example of applying one step of the wavelet transform to an image of vegetables on a market stall. The initial image is $N \times N$ ($N = 256$) and decomposed into 4 sub-images of equal size $N/2 \times N/2$, with a low-frequency approximation and detail coefficients detecting horizontal transients in the top right, vertical transients in the bottom left, and "diagonal" transients in the bottom right. A new iteration was performed on the low-frequency sub-image, resulting in 4 new sub-images of dimension $N/4 \times N/4$. The Haar wavelet ("db1") was used.

new, even more averaged approximation and 3 sub-images of "details". The reconstruction is done by adding the "details" obtained at different scales to the obtained low-frequency image.

Now let's consider image denoising. The process indicated for the 1D case is applied as-is in the 2D case. An example using the original image from Figure 11 is shown in Figure 12. The initial image (512×512) on the left has pixel values in the interval $[0, 1]$. The middle image is the result of adding Gaussian white noise with a moderate σ of 0.1, resulting in a PSNR¹⁴ of 20 dB. The image on the right shows the result of denoising using the thresholding method¹⁵ "hard" as described in Section 2.2.2, taking into account that in the threshold formula, N is replaced by N^2 , i.e., the total number of pixels. The wavelet used is the Haar wavelet, and the transformation was pushed to level 3. The PSNR of the denoised image is 28 dB.

Therefore, we have effectively denoised the image; however, the same zoomed portion of the images highlights that denoising "blurs" the contours and reduces the contrasts. This is where the limitation of 2D wavelet transformation with wavelets like "db" is pointed out. To study this limitation, we will use a certain type of images in the next section that control the regularity of contours and background.

2.2.4. Limit of classical wavelet analysis: C^α images. As observed during the denoising of a natural image, there is a phenomenon of blurring contours. To investigate this phenomenon, during the 2000s, "synthetic" images were generated with a background featuring a certain level of regularity controlled by a parameter α , akin to a typical contour within the image. The higher the value of α , the greater the regularity observed in both the background and the contour. These are called C^α images. Examples are shown in Figure 13.

The denoising of a C^2 image (i.e., $\alpha = 2$) is shown in Figure 14. It can be noted that the PSNR is much better than that obtained for a natural image of the same dimension. The evolution of the

¹⁴PSNR: *Peak Signal to Noise Ratio* defined as $10 \log_{10}(I_{max}^2 / \|x - x_{ref}\|^2)$ with $I_{max} = 1$ in our case.

¹⁵nb. other thresholding functions may give similar or worse results.

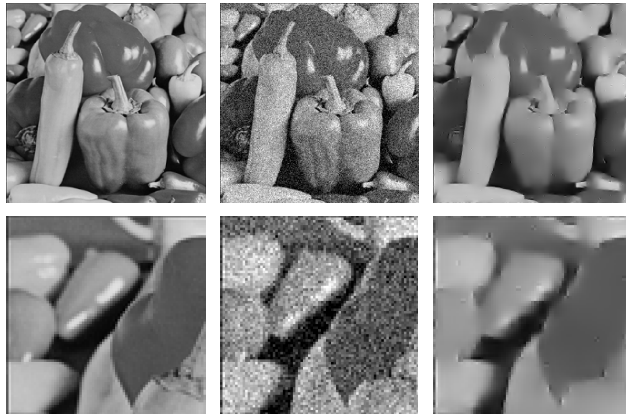


FIGURE 12. Left to right in the first row: the original image 256×256 with pixel values in the interval $[0,1]$, the noisy image ($\sigma = 0.1$, PSNR of 20 dB), and the denoised image (PSNR of 25.5 dB). The second row shows the same zoomed region of each image.

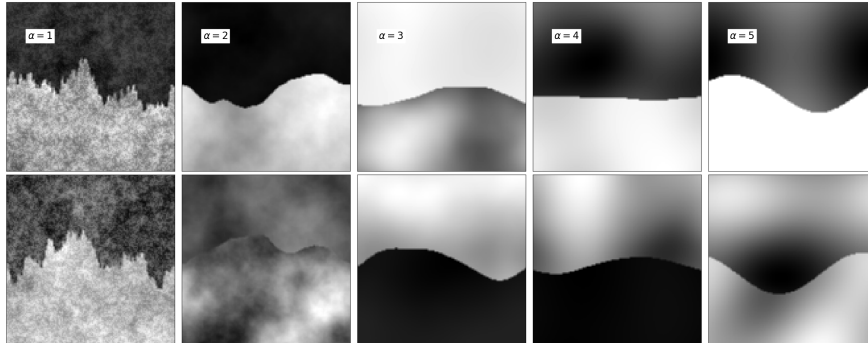


FIGURE 13. Examples of C^α images with identical α per column.

PSNR of the denoised image is depicted as a function of either the number of pixels or the regularity factor α in Figure 15. The $\log N$ scaling law, where N represents the number of pixels along one dimension of the image, can be elucidated as follows: when the size is increased by a factor of $\times 2$, the image can be filtered using, for example, a Gaussian kernel of size 2×2 , resulting in the original image size but with the noise variance reduced by a factor of 4. As PSNR is given by $-\log_{10}(\sigma)$, this indeed yields a $\log_{10} N$ scaling law. However, determining the exact law is more intricate, as is discerning the shape of the curves illustrating the denoised PSNR versus the noisy PSNR across the parameter α . We will revisit this topic in the section discussing denoising via deep neural networks.

Now, even though denoising is at work, it remains observed as for the natural image, a deterioration of the boundary between the two parts of the C^α image as can be seen in the zooms of Figure 14 (second row) and the difference between the original image and the denoised image. In fact, as shown by Le Pennec et al. (2007), this fundamentally stems from the fact that the support of the wavelets defined by equations 22, 24 does not adapt to the geometry of the image, especially that of the contours. A strategy developed in the 1995-2015 period roughly consisted of finding "directional" wavelets and establishing adapted thresholding algorithms.

2.2.5. Directional wavelets. As briefly illustrated in the previous section, the classical 2D Wavelet Transform (Eq. 22) does not adapt well to the geometry of images, especially to contours. An

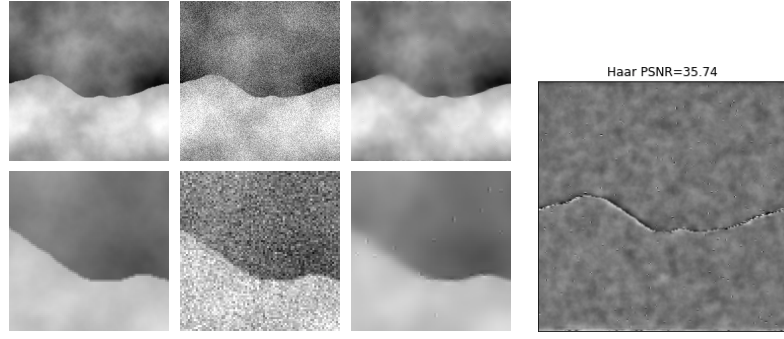


FIGURE 14. Left to right in the first row: the original C^2 image (256×256) with pixel values in the interval $[0.1]$, the noisy image ($\sigma = 0.1$, PSNR of 20 dB), and the denoised image (Haar wavelet ("db1") and Donoho et al.'s "hard" thresholding, with "soft" thresholding giving the same result). The second row shows the same zoomed region of each image. The rightmost image is the difference between the original and denoised images.

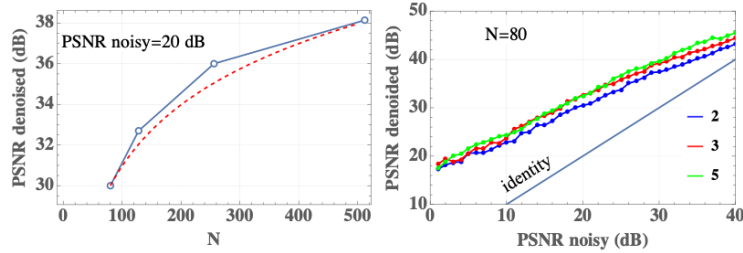


FIGURE 15. Left: the PSNR of a C^2 image denoised as a function of N (i.e., N^2 pixels) at $\sigma = 0.1$ or constant PSNR=20 dB of the noisy image (the red curve reflects a law of $constant + 10 \log_{10} N$). Right: the PSNR of C^α images $\alpha = 2, 3, 5$ (80×80) denoised as a function of the PSNR of the noisy image. The blue line marks the curve where the PSNR of the denoised image is identical to the PSNR of the noisy image (i.e., identity).

improvement would be to design directional analyses. The subject is very vast, so I will only take a few cases to illustrate.

One possible solution is to use the Morlet/Gabor wavelet transposed in 2D:

$$(25) \quad \begin{aligned} \psi(u_1, u_2) &= \left(-e^{-\frac{\xi^2}{2}} + e^{i\xi u_1} \right) e^{-\frac{u_1^2 + u_2^2}{2\sigma^2}} \\ \widehat{\psi}(\omega_1, \omega_2) &= \pi\sigma^2 e^{-\frac{1}{2}\sigma^2\omega_2^2} \left(e^{-\frac{1}{2}\sigma^2(\omega_1 - \xi)^2} - e^{-\frac{1}{2}(\xi^2 + \sigma^2\omega_1^2)} \right) \end{aligned}$$

The parameter σ plays a role in the characteristic width of the wavelet, while ξ sets the position of the power maximum in Fourier. An illustration is given in Figure 16. Now, one can change the scale λ as we have already done previously (similarly for translation) which we take dyadic ($\lambda = 2^j$ with $j \in \mathbb{Z}$), but we can also apply a rotation by an angle θ . It follows¹⁶

$$(26) \quad \psi_{j,\theta}(u) = 2^{-2j} \psi(2^{-j} r_\theta \cdot u) \implies \widehat{\psi}_{j,\theta}(\omega) = \widehat{\psi}(2^j r_{-\theta} \cdot \omega)$$

Then, by combining a collection of wavelets with different parameters j and θ , we can cover the Fourier plane. Figure 17 illustrates this point. Of course, one can adapt the base wavelet and the number of rotations to fill in any holes left here just to make the different associated "blobs" visible.

¹⁶nb. $r_\theta = \begin{pmatrix} \cos \theta & -\sin \theta \\ \sin \theta & \cos \theta \end{pmatrix}$.

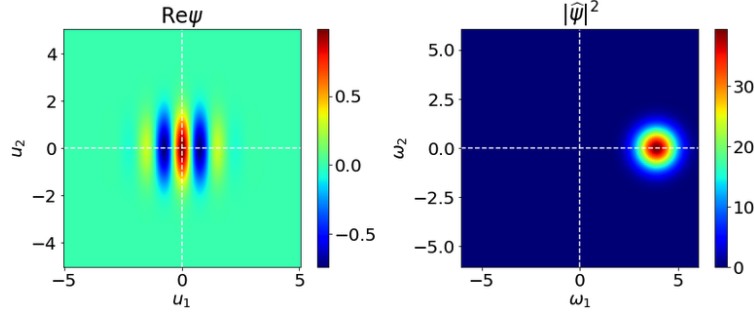


FIGURE 16. Basic 2D wavelet (Eq. 25) with its Fourier spectrum localized around $\omega_1 \approx \xi$ ($\sigma = 1$, $\xi = 5/4\pi$) and its power in the $\omega_1 \leq 0$ plane being null.

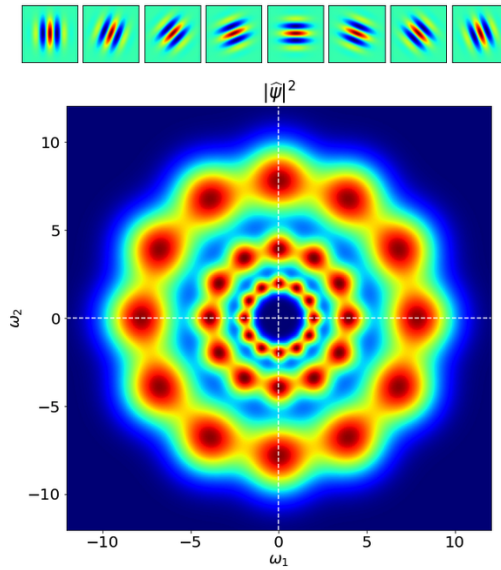


FIGURE 17. Top: wavelet (real part) undergoing rotations $k\pi/8$ with $k \in \{0, \dots, 7\}$. Bottom: coverage of part of the Fourier plane by collecting the spectra of several wavelets with scale factor $j = (-1, 0, 1)$ and having undergone multiple rotations of 30deg.

However, as in 1D, to cover the low frequencies (the central zone, $\omega \sim (0, 0)$), we resort to using a low-pass filter $\phi(\omega)$ such as a simple Gaussian.

So finally, the image (signal) is passed through a set of bandpass filters and a low-pass filter ($\theta_k = \pi k/K$)

$$(27) \quad Wx = ((\psi_{j,\theta_k} * X)_{j \in \{j_{min}, \dots, j_{max}\}, k \in \{0, \dots, K-1\}}, \phi * X)$$

which allows the signal to be analyzed at all scales and orientations. It is also necessary to take into account translations in real space in order to have a complete view of the transients throughout the entire image. Note that a particular orientation of a wavelet is sensitive to transients along the perpendicular axis.

From an image, using different orientations and spatial translations, it is "split" into all these filtering channels, and we obtain sub-images that can be represented as in Figure 18. It can be noticed that at each scale, the orientation of the wavelets makes orthogonal transitions visible in the original image. Thus, the boundaries between areas of equal intensity are detected, which

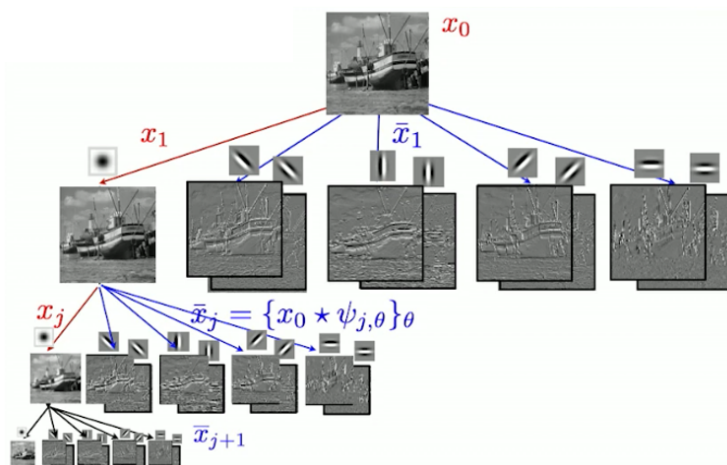


FIGURE 18. Successive cascade of applications of low-pass (ϕ) and band-pass ψ filters at different scales and four rotations $\{0, \pi/4, \pi/2, 3\pi/4\}$ (note the utilization of both the real and imaginary parts of the filters). At a given scale and rotation, all coefficients obtained by translations are collected to reconstruct sub-images. At each change of scale, a pooling/averaging operation is performed by a factor of 2 in both directions, changing the size of the sub-images. Dark areas indicate zones where the coefficients are zero.

are the transient phenomena sought. This scale/orientation decomposition is implemented in the so-called *scattering networks* architecture (Bruna and Mallat, 2013) and their developments as in references Zarka et al. (2020, 2021). For applications in cosmology, see for example Cheng et al. (2020, 2024).

2.2.6. *Wavelets aiming to adapt to geometry.* In the same vein as the previous orientable wavelets, orientable wavelets of the *steerable wavelet* type were developed in the 1990s (see, for example, Simoncelli and Freeman (1995)). This marked the second generation of wavelets. An example is given in Figure 19 for a single decomposition scale. Given an input image, it is first divided into a high-frequency part and a low-frequency part, then band-pass filters are applied to the low-frequency part of the image to detect edges at different angles. Regarding denoising, it is necessary to estimate the noise of the different coefficients in order to apply effective thresholding and restore a denoised image (see, for example, the BLS-GSM method by Rajaei (2014)).

Another type of orientable wavelets uses the concept of *ridgelets* (Donoho, 2000; Candès and Guo, 2002), defined as follows: if $\psi(x)$ is a "traditional" wavelet, then the family of functions

$$(28) \quad r_{s,b,\theta}(x_1, x_2) = s^{-1/2} \psi((x_1 \cos \theta + x_2 \sin \theta - b)/s)$$

are constant along the line $x_1 \cos \theta + x_2 \sin \theta = \text{constant}$. A version that contributed to the development of edge detection, compression, and denoising algorithms was introduced later (Candès and Donoho, 2000). The idea is as follows. In the classical case to obtain the wavelet coefficient (at a certain scale, without translation) of a function f , convolution is performed as follows:

$$(29) \quad \int f(x_1, x_2) 2^j \psi(2^j x_1, 2^j x_2) dx_1 dx_2 = \int 2^{-j} f_{2^{-j}}(x_1, x_2) \psi(x_1, x_2) dx_1 dx_2$$

with

$$(30) \quad f_s(x, y) = f(s x, s y)$$

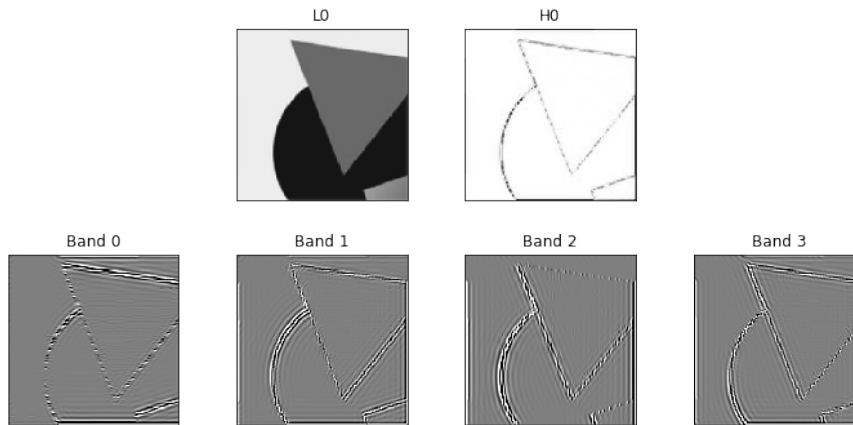


FIGURE 19. Example of image decomposition using the *steerable wavelet* method. The band-pass filters detect edges oriented at different angles ($0, \pi/4, \pi/2, 3\pi/4$).

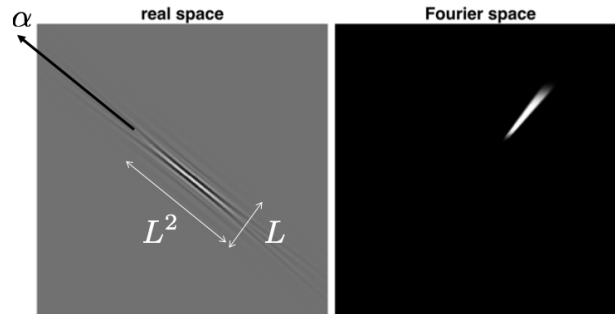


FIGURE 20. Example of a *curvelet* in real space (left) and schema of the support in Fourier space. *CurveLab*-2.1.3 with $((s, w) = (5, 15))$.

thus there is identical scaling on both coordinates. However, if we consider the function $f(x, y) = \mathbf{1}_{y \geq x^2}$, the scaling transformation $f(sx, s^2y)$ seems most appropriate (*parabolic scaling*). In fact, this type of scaling transformation needs to be performed locally in the "tangent-normal" frame. This is where the *curvelets* are developed, an example of which is shown in Figure 20 in both the real space and the Fourier space. Fast transformation algorithms have emerged and are described in the articles by Starck et al. (2002); Candès et al. (2006); Eslahi and Aghagolzadeh (2016) (e.g., *CurveLab*¹⁷, and *ACT*¹⁸). In astro-cosmology, there are numerous applications such as Starck, J. L. et al. (2003); Woiselle et al. (2010); Hergt et al. (2017).

2.2.7. Generalization of Curvelets and Bandlets. A generalization of *curvelets* was implemented by Le Pennec and Mallat (2005b) to adapt to contour geometries and exploit the regularity of the image (or function in general) along contours. In terms of shape regularity, the classical transformation exploits possible isotropy regularity over square domains at different scales. Curvelets exploit regularity along quadratic contours, while *bandlets* generalize the concept (Mallat and Peyré, 2007). An example is shown in Figure 21. Many applications have been developed, including image compression (Le Pennec and Mallat, 2005a) and denoising, as in the articles by Le Pennec et al. (2007) (French) and Vergara et al. (2008); Mclaughlin et al. (2015). The article by Zhang et al. (2019) provides an application in astronomy, and Ferroukhi et al. (2019) in the field of medical imaging.

¹⁷<http://www.curvelet.org>

¹⁸<https://fr.mathworks.com/matlabcentral/fileexchange/112215-act>

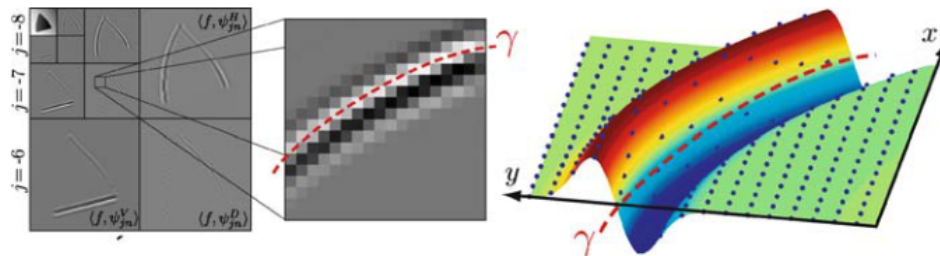


Fig. 13 Wavelet coefficients at a given scale 2^j are uniformly sampled from a regularized function $f * \psi_j^k(x)$ shown on the right

FIGURE 21. Example of decomposition into *bandlets*. Extracted from Mallat and Peyré (2007).

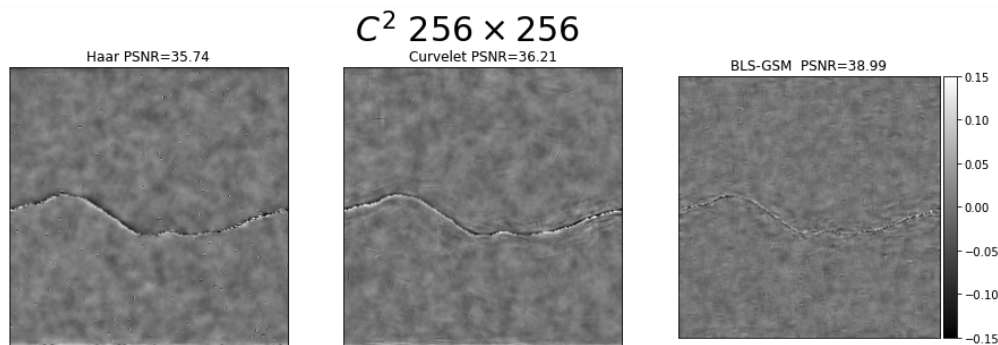


FIGURE 22. Images showing the difference between the original and denoised images (the added noise results in a PSNR of 20 dB): the left one is taken from Figure 14, the middle one is obtained using *curvelets*, and the right one is from the BLS-GSM code.

Regarding the denoising of C^2 images, what about it? Figure 22 presents results in addition to those reported in Figure 14, obtained with *curvelets* and *steerable wavelets*, as well as the thresholding methods used in the codes¹⁹. I couldn't find a code implementing *bandlets* which would have achieved an optimum (see Sec. 3.4 Eq. 56).

It is clear that while the PSNR of denoised images is better for directional wavelets, the "border zone" is still the least well denoised. This was the state of the art around 2015. Neural networks will change the game, as they did for image classification, then extended to image processing in general, as well as sound processing, speech, and then language-related tasks, etc.

3. DENOISING WITH DEEP NEURAL NETWORKS

3.1. Architecture: Some Reminders. I won't delve into the entire zoo of neural networks, nor their history. The reader can consult the following survey by Sze et al. (2017) even not up-to-date for a basic overview of some Deep neural networks concepts. It's worth noting that denoising with neural networks (Tang et al., 2012) emerged shortly before the advent of AlexNet (Krizhevsky et al., 2012). Networks used for denoising, for example, include the DnCNN architecture by Zhang et al. (2017) and U-Net²⁰ by Ronneberger et al. (2015) (Fig. 23).

These two networks are composed of layers with specific actions:

¹⁹CurveLab (MATLAB code) and BSM-GSL (<https://www.ipol.im/pub/art/2014/86/>)

²⁰Note: This network was originally designed for medical image segmentation. Its multi-scale structure is also relevant for denoising.

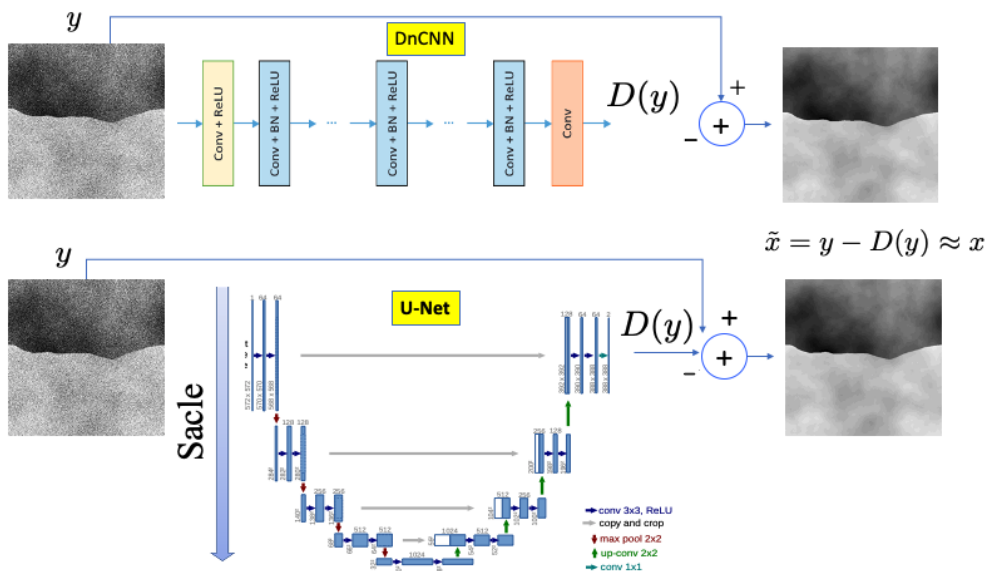


FIGURE 23. Architectures of deep networks used for denoising.

- (1) Convolutional layer: If we denote $(H_{\text{in}}, W_{\text{in}}, C_{\text{in}})$ as the dimensions of the input tensor and $(H_{\text{out}}, W_{\text{out}}, C_{\text{out}})$ for the output tensor, and consider a batch of convolutional kernels \mathcal{K} of size $K \times K$, then the values of the output tensor are calculated as follows²¹:

$$(31) \quad T_{i,j,k}^{\text{out}} = \sum_{c=1}^{C_{\text{in}}} \sum_{(u,v) \in \Delta_K} \mathcal{K}_{k,c,u+s,v+s} \times T_{i+u,j+v,c}^{\text{in}} \quad \text{with } s = \lfloor K/2 \rfloor, \quad \Delta_K = \{-s, \dots, s\}^2$$

One can observe at first glance that not only does this operation act in the two spatial dimensions but also mixes the input channels. It's an operation to be visualized in 3D (Fig. 24), where the part concerning the dimensions (H, W) resembles a wavelet decomposition in every aspect except that the filters are learned. However, it's important to note that the operation on the channels leads to the remarkable properties of convolutional networks. If this operation is removed, the performance degrades significantly (Zarka et al., 2020)²².

- (2) Batch Normalization layer: This operation conditions the Hessian matrix of the convolution with respect to its parameters by performing the substitution

$$x_i \rightarrow x'_i = \frac{x_i - M}{S}$$

where M and S^2 are the empirical mean and variance.

- (3) Pointwise Non-linear Activation: Such as a Rectified Linear Unit (ReLU) $\rho(x) = \max(0, x)$. These nonlinearities are essential; otherwise, the network operation would be purely linear, incapable of separating "XOR" type samples. One other argument concerns the non-extinction of gradients.
- (4) Pooling layer: Average, max, etc.
- (5) Deconvolution and upsampling layer in the case of contracting and expansive architectures like in the case of U-Net.

If the architecture of DnCNN presents a linear sequence of blocks (convolution, batch-norm, ReLU), that of U-Net proceeds in two parts: the first (contracting) chains convolutions and subsamplings

²¹To simplify, I haven't included a possible bias b_k .

²²see "Scat alone" results in Tab. 1.

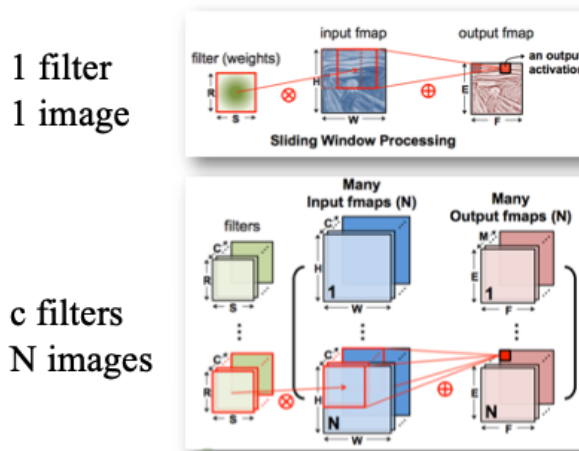


FIGURE 24. Illustration of operations performed by convolutional layers. There are three particular dimensions of the tensors (Height, Width, and number of "channels"). The operation on the coordinates (H,W) constitutes a "classic" convolution, and summing over the "channels" gives the remarkable properties of CNNs.

as for a wavelet decomposition, while the second (expansive) performs the inverse transformation. There are other architectures that proceed in this way, such as Variational Auto-Encoders (Kingma and Welling, 2013). What distinguishes U-Net is the fusion at each scale of the results of the two phases. This mechanism, called "skip connection", merges information from higher resolution with information from lower resolution. This feature allows correlating information at different scales.

3.2. Learning the noise. Regarding the denoising task, the model (e.g., U-Net) denoted D_θ (with θ being the set of parameters to optimize) is used to learn *the noise*. That is, if we denote y as the sample at the input of the network corresponding to the noisy signal and $D_\theta(y)$ as the output, then

$$(32) \quad \tilde{x}(y) = y - D_\theta(y)$$

is constrained to match the noise-free signal x . This means that the cost function to minimize is the *mean square error*, such that if we have n samples $\{x_i, y_i\}_{i \leq n}$ then:

$$(33) \quad \theta^* = \operatorname{argmin}_\theta \sum_{i=1}^n \|x_i - \tilde{x}(y_i)\|^2$$

The models are trained with all levels of noise $\sigma \in [0, 1]$, knowing that the pixels of the x_i are also in $[0, 1]$. It should be noted that training with only one level of noise gives poorer results. In the following, I will only consider the results concerning the U-Net architecture, but they are similar to those obtained with DnCNN (Kadkhodaie et al., 2024). A peculiarity used by the authors of this article is to *remove bias terms* from the layers (convolution and batchnorm), which gives the network the property of being *first-order homogeneous* in the sense of differentiable functions from $\mathbb{R}^n \rightarrow \mathbb{R}^n$. Euler's theorem then tells us that

$$(34) \quad D_\theta(y) = (\nabla_y D_\theta(y)) y$$

where the Jacobian of $D_\theta(y)$ appears.

The denoising result of a C^2 image (80×80) to which Gaussian noise with a PSNR of 20 dB ($\sigma = 0.1$) was added is shown in Figure 25. The network was trained with 100,000 images. These results should be compared to those obtained in Section 2.2.5 taking into account the reduction in size²³ required for training the U-Net. The quality of the reconstruction by the neural network can

²³Refer to the curves in Figure 15 to appreciate the change in PSNR with size.

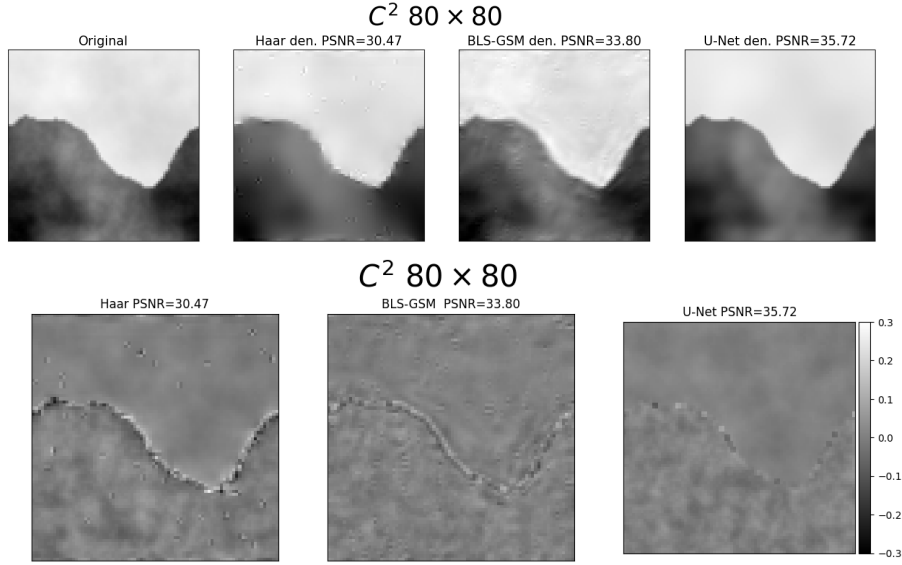


FIGURE 25. An image C^2 contaminated by Gaussian noise (PSNR of 20 dB, pixel values of the noise-free image are in the range $[0, 1]$) denoised by methods using a classical method (denoted "Haar") discussed in Section 2.2.4, a method using directional wavelets described in Section 2.2.5, and by the U-Net network. The second row shows the difference between the noise-free image and the respective denoised images (the same grayscale is applied for all three images). The PSNR of the denoised images for each method is mentioned. Beyond the PSNR value, the quality of the boundary reconstruction favors the neural network (trained here with 100,000 images).

also be appreciated as a function of the regularity order α of C^α images and the level of added noise (input PSNR) (Fig. 26). The curves from Figure 15 are reported here for comparison. It is noted that the network performs better especially at the boundary, and it behaves better as the regularity order increases.

Questions arise: why do networks like U-Net perform significantly better than previously developed methods? What do they learn? Is it generalizable to other types of images? What about the size of the training image batch? To address these questions, I will heavily rely on recent work by Kadkhodaie et al. (2024).

3.3. What does the network learn? Orthogonal basis and thresholding. If we consider the definition (Eq. 32) of the estimated $\tilde{x}(y)$ of the noise-free signal x from the noisy signal y , and take into account the homogeneous nature of the network's response (Eq. 34), then we can write

$$(35) \quad \tilde{x}(y) = (\text{Id} - \nabla_y D_\theta(y)) y = \mathcal{O}_\theta(y) y$$

By diagonalizing the operator $\mathcal{O}_\theta(y)$, denoting $(\lambda_k(y), e_k(y))_k$ the set of eigenvalues and eigenvectors, we can express y in this basis by denoting $c_k(y) = \langle y, e_k(y) \rangle$:

$$(36) \quad y = \sum_k c_k(y) e_k(y)$$

Similarly, the denoised signal decomposes as

$$(37) \quad \tilde{x}(y) = \sum_k \lambda_k(y) c_k(y) e_k(y)$$

This relationship is reminiscent of the thresholding formulas in Eqs. 4, 17 while maintaining adaptivity to the geometry of y as seen for wavelets because the thresholding function $\rho(c_k(y)) = \lambda_k(y) c_k(y)$

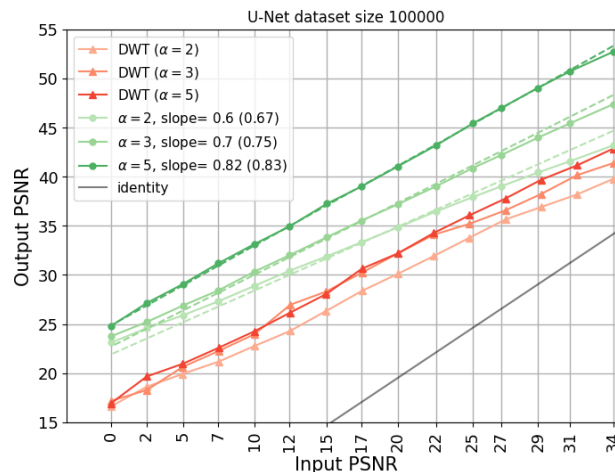


FIGURE 26. Evolution of the PSNR of denoised images as a function of the regularity order α of noise-free images and the injected noise level. The networks (one per α value) were trained with 100,000 images each. The "DWT" points are those obtained with the classical wavelet denoising method (Haar, Donohoa et al. hard thresholding) from Figure 15. The dashed lines are discussed in Section 3.4.

depends on y . Thus, the network learns not only the basis but also the thresholding to apply to remove the noise.

In practice, what does this give us? Obtaining the eigenvalues and eigenvectors of $\mathcal{O}_\theta(y)$ is done via the Singular Value Decomposition (SVD) from an image y with, for example, noise such that $\sigma = 0.1$ (20 dB). The results are shown in Figures 27 and 28 for C^α images with $\alpha = 2$ and 5. First, we notice that the dot products decrease rapidly²⁴, indicating that we are indeed dealing with a sparse decomposition. The eigenvalues also decrease rapidly, exploiting sparsity well, especially since their clear decrease is noticed for $k \gtrsim 10^2$, i.e., as soon as the noise becomes noticeable. The most surprising aspect is the images of the eigenvectors: they are oscillating functions both along the contours and in the uniformly regular regions of the image (without crossing the boundary). In short, they adapt to the geometry.

These oscillating functions resemble solutions of a Laplace equation; they are called *geometry-adaptive harmonic basis* (GAHB). It can be seen that these bases are quite different from those used in Section 2. It must be understood that GAHB bases are adaptive; the basis vector depends on the signal ($e_k(y)$), whereas wavelet bases (or other "curvelets/bandlets, etc.) are not adaptive; the basis vector is known *a priori* (e_k). This is to be differentiated from the sparse nature, where the decomposition coefficients concentrate on local peculiarities (transients) of each signal: wavelet bases are sparse, while the Fourier basis is not for signals with transients.

3.4. Prediction of oracles and practical case. To understand the behavior of the network when performing denoising, let's take a small detour through a classical analysis called "oracles". If we take the expression of the denoised signal (Eq. 37), then the mean squared error (fixed signal x , noise $z \sim \mathcal{N}(0, \sigma^2)$, $y = x + z$) is given by:

$$(38) \quad \mathcal{E} = \mathbb{E}_z[\|x - \tilde{x}(y)\|^2] = \sum_k \mathbb{E}_z[(\langle x, e_k(y) \rangle - \lambda_k(y) \langle y, e_k(y) \rangle)^2]$$

To simplify, let's consider that $e_k(y)$ is independent of y , as if we were in a fixed orthonormal basis like the wavelet bases in Section 2.2. Let $c_k(x) = \langle x, e_k \rangle$ and similarly for $c_k(y)$ and $c_k(z)$. Note

²⁴Reminder: they are organized according to the decreasing values of the eigenvalues.

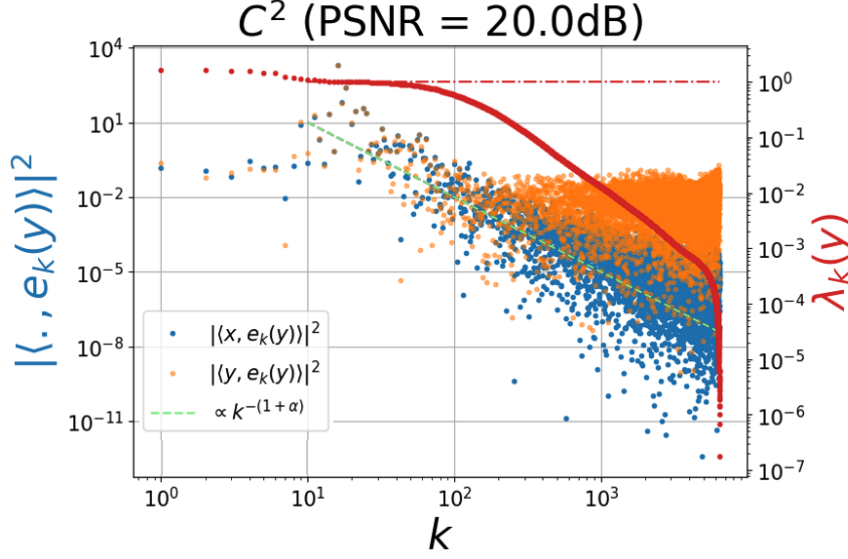


FIGURE 27. Left scale: evolution of the coefficients $c_k^2(x) = |\langle x, e_k(y) \rangle|^2$ (blue dots) and $c_k^2(y)$ (orange dots) as a function of k . The presence of noise (PSNR of 20 dB, $\sigma = 0.1$) is noted from $k \approx 10^2$. The dashed green curve indicates a scale law of $1/k^{1+\alpha}$ (here $\alpha = 2$) followed by the coefficients $c_k^2(x)$ (see Sec.3.4). Right scale: evolution of the eigenvalues $\lambda_k(y)$ (red dots) which serve as thresholding factors for the coefficients $c_k^2(y)$, with a clear decrease for $k \approx 10^2$.

that by linearity $c_k(y) = c_k(x) + c_k(z)$, so we have

$$\begin{aligned}
 \mathcal{E} &= \sum_k \mathbb{E}_z [(c_k(x)(1 - \lambda_k(y)) - \lambda_k(y)c_k(z))^2] \\
 (39) \quad &= \sum_k \{ c_k^2(x) \mathbb{E}_z [(1 - \lambda_k(y))^2] - 2c_k(x) \mathbb{E}_z [c_k(z)(1 - \lambda_k(y))\lambda_k(y)] + \mathbb{E}_z [(\lambda_k(y)c_k(z))^2] \}
 \end{aligned}$$

At this stage, we have a problem to continue the calculation because $\lambda_k(y)$ implicitly depends on z . So, we will use an *oracle* which will give us $\lambda_k(x)$ instead. The result will be necessarily optimistic. It should also be noted that any decomposition of white Gaussian noise $\mathcal{N}(0, \sigma^2)$ over any orthonormal basis leads to random values of the coefficients according to $\mathcal{N}(0, \sigma^2)$. Therefore, $\mathbb{E}_z [c_k(z)] = 0$ and $\mathbb{E}_z [c_k^2(z)] = \sigma^2$. Then we have

$$\begin{aligned}
 \mathcal{E} &= \sum_k \{ c_k^2(x)(1 - \lambda_k(x))^2 - 2c_k(x)(1 - \lambda_k(x))\lambda_k(x)\mathbb{E}_z [c_k(z)] + \lambda_k^2(x)\mathbb{E}_z [c_k^2(z)] \} \\
 (40) \quad &= \sum_k \{ c_k^2(x)(1 - \lambda_k(x))^2 + \sigma^2 \lambda_k^2(x) \}
 \end{aligned}$$

Minimizing such an error amounts to minimizing each term, which leads to the prediction of the oracle:

$$(41) \quad \lambda_k^{om}(x) = \frac{c_k^2(x)}{c_k^2(x) + \sigma^2} \quad \Rightarrow \quad \mathcal{E}^{om} = \sum_k \frac{\sigma^2 c_k^2(x)}{c_k^2(x) + \sigma^2} = \sigma^2 \sum_k \lambda_k^{om}(x)$$

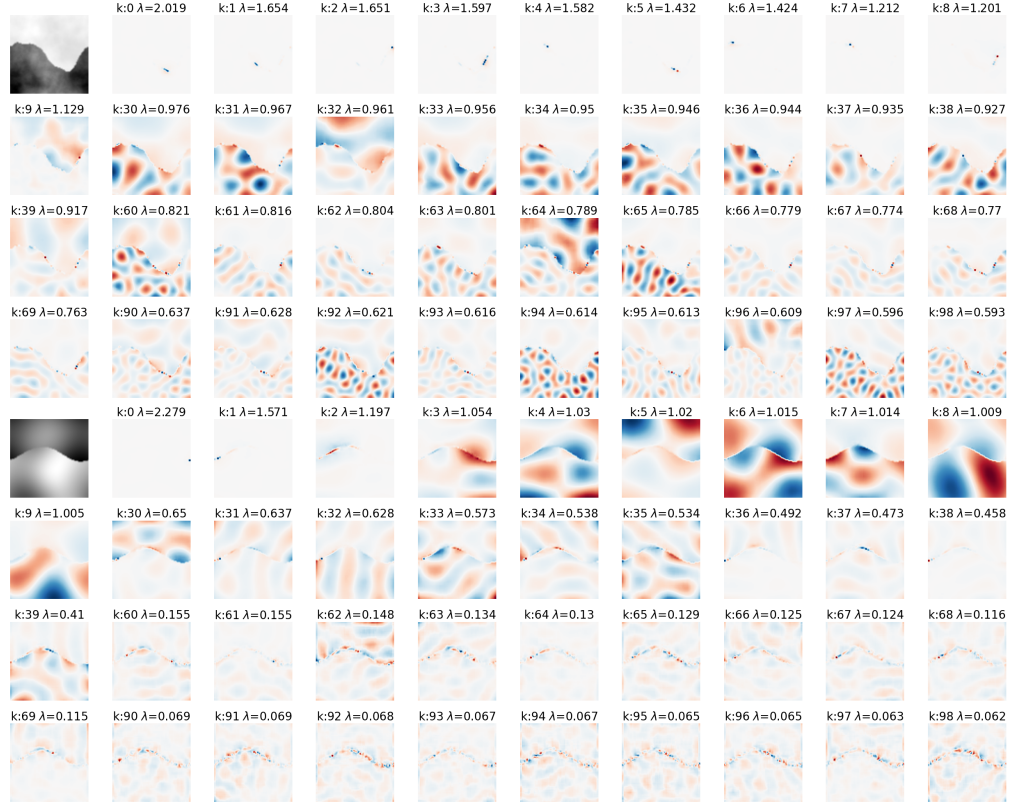


FIGURE 28. Some eigenvectors $e_k(y)$ for the case of a C^2 image (first four rows) and a C^5 image (last four rows).

Looking at equation 40, one might think of a harsher oracle that would use an adaptive "hard" thresholding (Eq. 15)

$$(42) \quad \lambda_k^{oh}(x) = \begin{cases} 1 & c_k^2(x) \geq \sigma^2 \\ 0 & \text{otherwise} \end{cases}$$

Let's re-index the coefficients $c_k(x)$ in a decreasing order such that

$$(43) \quad c_1(x) \geq c_2(x) \geq \dots \geq c_M(x) \geq \sigma^2 \geq c_{M+1}(x) \dots$$

The expression of the mean squared error of this oracle is equal to

$$(44) \quad \mathcal{E}^{oh} = \sum_{1 \leq k \leq M} \sigma^2 + \sum_{k \geq M+1}^{k_{\max}} c_k^2(x) = \sum_k \min(\sigma^2, c_k^2(x)) = M\sigma^2 + \|x - x_M\|^2$$

where for the last expression, we simply expressed that x_M is the approximation of x with the first M coefficients (re-indexed), and $k_{\max} = N^2$ in the case of an $N \times N$ image. Note that M is the cardinality of the following set:

$$(45) \quad M = \text{Card}\{k / c_k^2(x) \geq \sigma^2\}$$

We can relate \mathcal{E}^{oh} and \mathcal{E}^{om} , because $\forall(a, b) \in \mathbb{R}^+$ we have

$$(46) \quad \min(a, b)/2 \leq \frac{ab}{a+b} \leq \min(a, b)$$

thus

$$(47) \quad \mathcal{E}^{oh}/2 \leq \mathcal{E}^{om} \leq \mathcal{E}^{oh}$$

Therefore, up to a factor of 2, we can write that

$$(48) \quad \mathcal{E}^{om} \sim \mathcal{E}^{oh} = M\sigma^2 + \|x - x_M\|^2$$

This is a classical result of the behavior of the mean squared error of denoising in an orthonormal basis (Mallat, 2008).

The first observation is that if the coefficients $c_k(x)$ are zero for $k > M$, then the estimation error $\|x - x_M\|^2$ is zero, and the denoising error is minimal, equal to $M\sigma^2$ (corresponding to the variance of M independent random variables). This indicates that the more sparse the representation of the (noise-free) signal is (M small), the better denoising can be achieved.

We can also provide an estimate of the convergence rate of \mathcal{E}^{oh} (\mathcal{E}^{om}) in the case of a power-law decay of the coefficients (Kadkhodaie et al., 2024):

Theorem 3. *If there exist three strictly positive constants c_1, c_2, p such that*

$$(49) \quad c_1 k^{-(p+1)} \leq c_k^2(x) \leq c_2 k^{-(p+1)} \quad \Rightarrow \quad \mathcal{E}^{oh} \sim \sigma^{2p/(1+p)}$$

Now, to address the real case, we can't use the coefficients $c_k(x)$ as the oracle, since the signal x is unknown to us. Therefore, we can only use thresholding on the coefficients $c_k(y)$:

$$(50) \quad \lambda_k^T(y) = \begin{cases} 1 & c_k^2(y) \geq T^2 \\ 0 & \text{otherwise} \end{cases}$$

while still considering a fixed orthonormal basis. In fact, σ is replaced by T , and we can follow the previous developments, leading to

$$(51) \quad \mathcal{E}^T = M T^2 + \|x - x_M\|^2$$

with $M = \text{Card}\{k / c_k^2(y) \geq T^2\}$, similar to expression 45. The problem then boils down to finding the best threshold in the given basis. This is where the result of D. L. Donoho and I. M. Johnstone (Donoho, 2000) provides a practical solution that we have already used (e.g., Sec. 2.2.2):

Theorem 4. *(Donoho & Johnstone)*

If $T = \sigma\sqrt{2\log d}$ with d being the size of the signal, then²⁵

$$(52) \quad \mathcal{E}^T \leq C_d(\sigma^2 + \mathcal{E}^{oh})$$

with $C_d = (1 + 2\log d)$ and $\mathcal{E}^{oh} = \sum_k \min(\sigma^2, c_k^2(x))$. Moreover, C_d and T are asymptotically optimal.

Therefore, when $d \gg 1$ (which is the case), then up to a constant, with the above thresholding, we can achieve oracle performance. Thus, we can write (C being a constant)

$$(53) \quad \mathcal{E}^T \leq C\sigma^{\frac{2p}{1+p}}$$

Now, Korostelev and Tsybakov (1993) have shown that for C^α type images, the optimal quadratic error is such that

$$(54) \quad \mathcal{E}^{optim} \leq C\sigma^{\frac{2\alpha}{1+\alpha}}$$

which means that one can try to find a basis such that

$$(55) \quad |\langle x, e_k \rangle|^2 \sim k^{-(1+\alpha)}$$

Moreover, if we translate the scaling of \mathcal{E}^{optim} in terms of PSNR, the slope of the PSNR of the optimally denoised image as a function of the PSNR of the noisy image²⁶ is $\alpha/(1+\alpha)$.

²⁵the error by the oracle uses a "hard" thresholding given by σ .

²⁶incidentally equal to $-20 \log_{10} \sigma$.

This result motivated the search for orthonormal bases described in section 2.2.5. However, it is noteworthy that the result for "bandlets" (Sec. 2.2.5), which form the best sparse orthonormal basis for C^α images, gives (Le Pennec et al., 2007; Mallat and Peyré, 2008; Dossal et al., 2011) ($\sigma^2 \gg 1/d$)

$$(56) \quad \mathcal{E}^{bandlet} \leq C(|\log \sigma| \sigma^2)^{\alpha/(1+\alpha)}$$

There is an additional $|\log \sigma|$ factor compared to the optimal result of Korostelev and Tsybakov (1993).

Regarding the denoising result by the neural network, it is optimal: the decay of the coefficients $c_k^2(x)$ is as expected (Fig. 27) as well as the slope of the PSNR as illustrated in Figure 26. Since theory cannot access the offset, we cannot go further to know if we can do better in exploiting these results. However, by analyzing the result of Korostelev and Tsybakov (1993), it is indeed the detection of contours in the presence of noise, and the exploitation of the regularity of the function along these contours that are the keys (Dossal et al., 2011). It is clear that the network manages to capture these regularities. The next section will show another example.

3.5. The case of "celebrity" portraits. The next question arises: what are the performance of a **U-Net** for "natural" images? Kadkhodaie et al. (2024) used face images from the **CelebA** database²⁷ (Liu et al., 2015).

After training with 100,000 80×80 images, Figure 29 gives the results in a similar form to Figure 28. We can see that the eigenvectors again show the adaptation of the basis to the different contours present in the image. The decay (not shown) of the coefficients $c_k^2(x)$ is of the same nature as those obtained with C^α images. Other examples are presented in the article, including pictures of bedrooms.

3.6. Influence of the Database Size. In the previous sections, the **U-Net** networks were trained with 100,000 80×80 images. What if the size of the training batch is smaller? Figure 30 answers the question for an extreme case where the database consists of 10 images. The image used for denoising is an image from this same batch²⁸.

It can be observed that the denoising is almost perfect. However, it can be noticed that the eigenvectors do not exhibit the same property of oscillating functions respecting the contours of the image as observed in Figure 29. Similarly, Figure 31 shows that the decay of the coefficients $c_k^2(x)$ (i.e., $|\langle x, e_k(y) \rangle|^2$) as well as that of the eigenvalues $\lambda_k(y)$ is not satisfactory at all when $N = 10$: the decay is much less pronounced (lack of sparsity) and the thresholding much less effective.

Clearly, a sufficient number of training images is needed to obtain the qualities stated in the previous sections. Can we understand this?

3.7. What does the network learn? The score! In the previous sections, the signal x is considered as a deterministic process. We seek an approximation from the observation y which is the result of the corruption of x by additive white Gaussian noise: $y = x + z$ with $z \sim \mathcal{N}(0, \sigma^2)$. In this section, we will consider a probabilistic framework where x is the realization of a random variable with probability density $p_X(x)$. By the way, it might seem odd to consider that the images used in the previous sections are the result of random processes. However, we have been accustomed to the idea that systems with a large number of degrees of freedom are better understood through Statistical Physics since the beginning of the 20th century and the Boltzmann-Gibbs theory. And in this theory, a distribution of Gibbs is generically formulated underlying the process as follows:

$$(57) \quad p_X(x) = Z^{-1} e^{-U(x)}$$

²⁷<https://mmlab.ie.cuhk.edu.hk/projects/CelebA.html>

²⁸Otherwise, the results are even worse: the denoised image of a test image corresponds to a mixture that does not resemble the original image at all. However, for networks trained with 100,000 images, test images were used to produce denoising results and orthonormal bases.

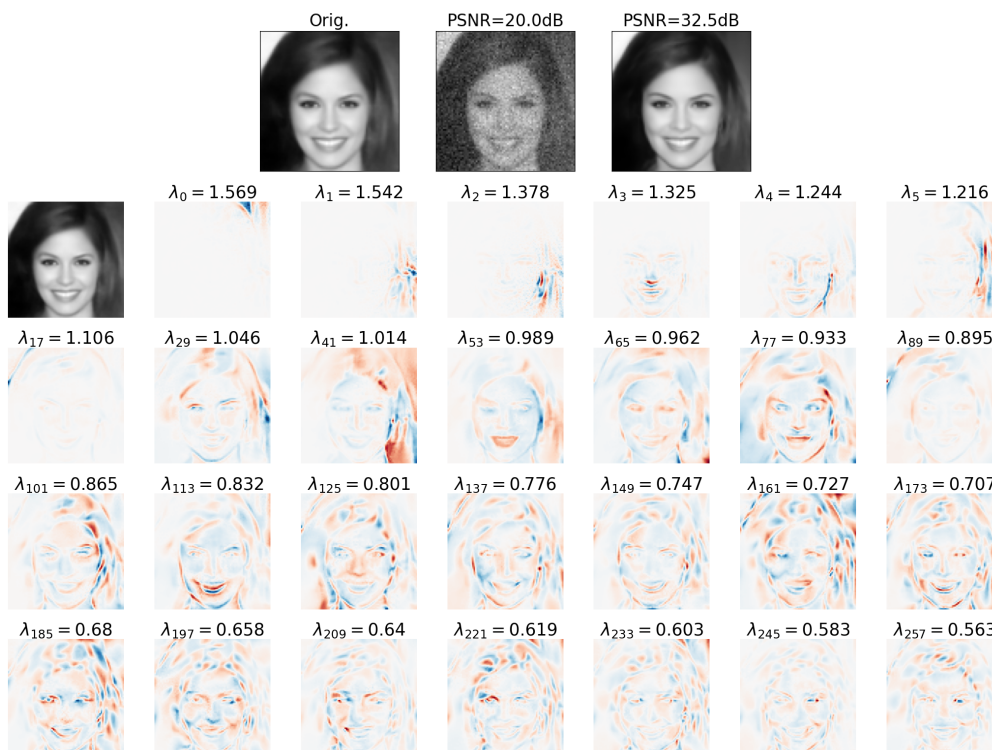


FIGURE 29. Top row: denoising of a typical face image. Bottom row: evolution of the eigenvectors of the signal projection base (see Fig. 28). Reminder: the size of the training batch is 100,000 80×80 images.

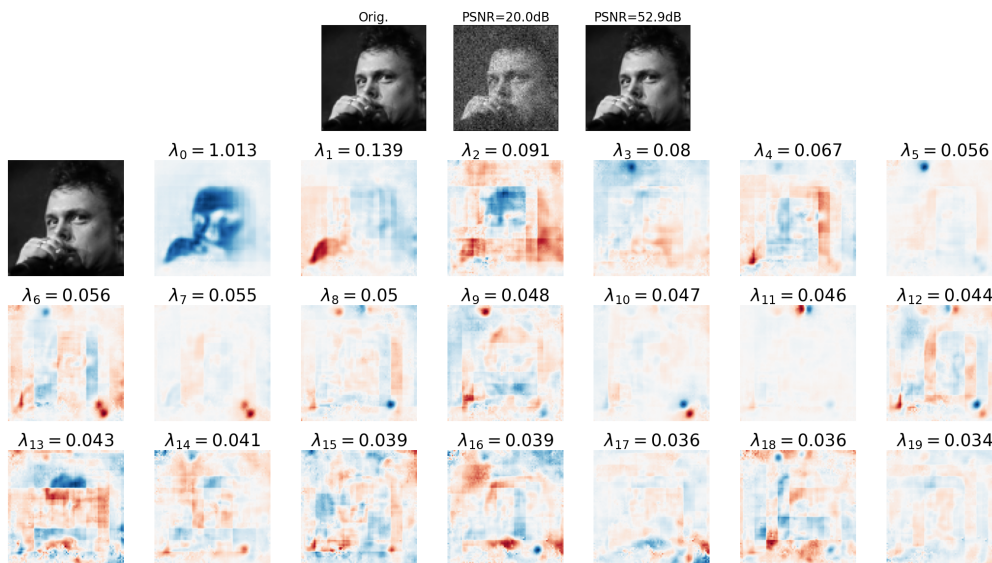


FIGURE 30. Same legend as Figure 29 but for a training batch size of 10 images instead of 100,000.

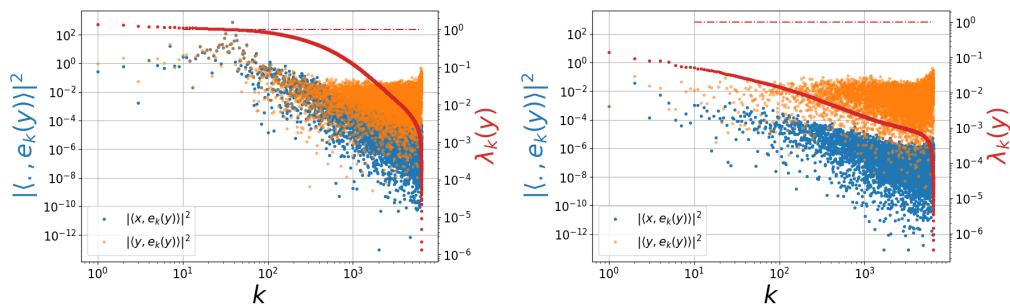


FIGURE 31. Evolution of $(c_k^2(x), c_k^2(y), \lambda_k(y))$ as a function of k similar to those in Figure 27 but obtained for a denoised face image by a network trained with 100,000 images on the left, and only 10 images on the right.

Moreover, the processes studied in Statistical Physics are certainly in most cases non-Gaussian ($U(x)$ does not have just a quadratic term in x) but they are ergodic. Thus, it is easy to make the implicit connection between an ergodic process and a probability distribution. However, there are non-ergodic processes, at least because they are not stationary, like face images. However, since the underlying process is not ergodic, this may indeed challenge our intuition shaped by Statistical Physics. Therefore, let's try to break free from this constraint, without completely disregarding it.

In this context, the search for $\tilde{x}(y)$, which best approximates the signal x , is done by minimizing the quadratic error in expectation over the two probability densities, that of y (via z) and that of x :

$$(58) \quad \tilde{x}(y) = \operatorname{argmin}_{\mathcal{O}} \mathbb{E}_{x,y} [\|x - \mathcal{O}(y)\|^2]$$

where \mathcal{O} is an operator from \mathbb{R}^d to \mathbb{R}^d (it transforms an image $d = N \times N$ into another image in the same space).

This is a Bayesian estimation whose following theorem gives the solution:

Theorem 5. *The Bayesian estimator of the denoised signal is given by ($i = 1, \dots, d$)*

$$(59) \quad \tilde{x}(y)_i = \mathbb{E}_x [x_i | y = (y_1, \dots, y_d)] = \int x_i p_i(x_i | y) dx_i$$

The main problem, even if we have a compact form, lies in the fact that $p_i(x_i | y)$, whether we like it or not, depends on the *a priori* $p_i(x_i)$ (for all $i = 1, \dots, d$). Moreover, the integral calculation must be performed in high dimension. This is why initially Wiener (1949) sought a linear operator of the form $\tilde{x}(y) = L.y$.

But as pointed out by Tweedie (1947); Herbert (1956); Miyasawa et al. (1961) and more recently by Raphan and Simoncelli (2011), for Gaussian white noise $\mathcal{N}(0, \sigma^2)$ independent of the unnoisy signal x , we have the following result independent of the prior on x :

Theorem 6. *The estimator $\tilde{x}(y)$ of the signal x , such that $y = x + z$ ($z \sim \mathcal{N}(0, \sigma^2)$), is given by*

$$(60) \quad \tilde{x}(y) = y + \sigma^2 \nabla_y \log p(y)$$

This theorem could be just as frustrating as the Bayesian estimator theorem invoking conditional probability, but it also tells us that if we have a good denoiser, like the well-trained **U-Net** network, then knowing $\tilde{x}(y)$ and the noise variance²⁹, then we have an estimator of the score $\nabla_y \log p(y)$ of the distribution of observables. And it is this ingredient that proves to be crucial for generating new samples from training images.

²⁹It could be estimated with the signal itself as we did in the context of denoising in wavelet bases for example.

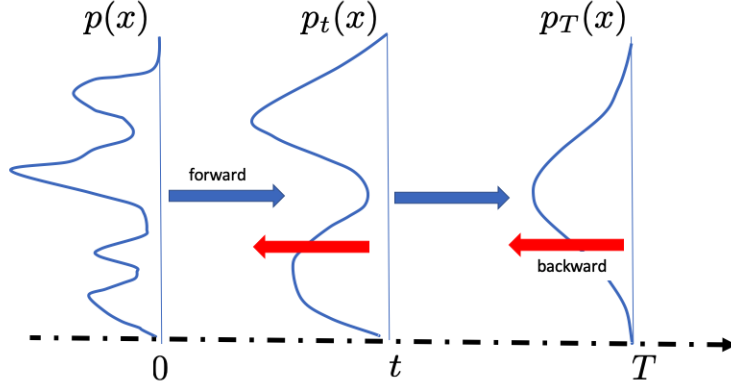


FIGURE 32. Evolution of the distribution $p(x)$ during the transformation steps indexed by t in the direction of adding noise (blue arrows), and if the process can be inverted (red arrows) then from a sample of $p_T(x)$ we obtain a new sample of $p(x)$.

3.8. Score-Based Generation. To generate samples from $p(x)$, we proceed as follows (see e.g., Chang et al. (2023)). Starting from a sample x assumed to be drawn from the distribution $p(x)$, we progressively transform it (steps indexed by $t \in [0, T]$) until the underlying distribution is very simple, namely a Gaussian with $\sigma = 1$. This is the *forward* process in Figure 32. The idea is then to reverse the process (the *backward* mode) by generating a new sample from a new instance of noise.

The transport process used in the Score Diffusion algorithm is the Ornstein-Uhlenbeck equation (Uhlenbeck and Ornstein, 1930). The *forward* process follows the following stochastic differential equation:

$$(61) \quad dx_t = -x_t dt + \sqrt{2} dB_t \quad t \in [0, T]$$

where dB_t is a Wiener process (Brownian motion). The discretization gives (constant time step δ):

$$(62) \quad x_{t+\delta} = (1 - \delta)x_t + \tilde{z} \quad \tilde{z} \stackrel{iid}{\sim} \mathcal{N}(0, 2\delta Id)$$

It is a Gaussian and Markovian process whose solution is given by

$$(63) \quad x_t = x_0 e^{-t} + \underbrace{(1 - e^{-2t})^{1/2}}_{\sigma_t} z \quad z \stackrel{iid}{\sim} \mathcal{N}(0, Id)$$

The associated probability density function is given by the expression

$$(64) \quad p_t(x_t) = \int p_t(x_t, x_0) dx_0 = \int p_t(x_t | x_0) p_0(x_0) dx_0$$

where according to the Fokker-Planck representation of the Ornstein-Uhlenbeck process, we have

$$(65) \quad p_t(x_t | x_0) = \frac{1}{(2\pi\sigma_t^2)^{d/2}} e^{-\frac{\|x_t - x_0 e^{-t}\|^2}{2\sigma_t^2}} = g_{\sigma_t}(x_t - x_0 e^{-t})$$

In fact, $p_t(x_t)$ is the result of the convolution of the initial distribution $p_0(x_0)$ with this Gaussian which gradually tends towards $\mathcal{N}(0, 1)$, producing a progressive smoothing that also makes $p_t(x_t)$ tend towards the normal distribution.

Now, let's move on to the *backward* process, which is also the result of a stochastic differential equation (damped Langevin):

$$(66) \quad dx_{T-t} = (x_{T-t} + 2\nabla_x \log p_{T-t}(x_{T-t})) dt + \sqrt{2} dB_t \quad t \in [0, T]$$

which in discrete form ($\delta > 0$ constant time step) gives the relation:

$$(67) \quad x_{t-\delta} = (1 - \delta)x_t + 2\delta s_t(x_t) + \sqrt{2\delta} z \quad z \stackrel{iid}{\sim} \mathcal{N}(0, Id)$$

where $s_t(x_t) = \nabla_x \log p_t(x_t)$ is the score.

Here, there are two possible approaches: either we have a model for p_t (e.g., Guth et al. (2022) in the case of generating φ^4 fields, for example) that can exploit regularity patterns and assumptions about correlations to provide a constrained parametric framework for learning the score, or we use a denoising neural network for the same purpose. So, imagine that we have a batch of input images (x_0), at each step t of the *forward* pass, we have new noisy images with variance σ_t , which can be used to train a network³⁰ like a **U-Net** to denoise them and thereby obtain the score $s_t(x_t)$ at step t . Then, starting from a pure noise instance (x_T), we perform the iterations of the *backward* process, and at $t = 0$ we obtain a new sample from p_0 .

The real question when we see such images produced by these generative models is: are we sampling from a probability density? In other words, has the model learned $p(x)$ with x being a face image, and what is the nature of this distribution p ? The alternative would probably be that the new images are sophisticated patchworks of database images? A first answer was given by Kadkhodaie et al. (2024).

3.9. Memorization vs Generalization. Generating new samples from a distribution $p(x)$ using the Score Diffusion method briefly described in the previous section raises questions. In particular, the quality of the generated images and their real novelty may be questionable. To try to answer both questions, consider the following experiment: prepare two disjoint sets of N images ($(B_1(N), B_2(N))$) from the same database (i.e., CelebA), and train two **U-Net** networks ($S_1(N), S_2(N)$), $S_i(N)$ with $B_i(N)$. This is repeated for batch sizes $N = 1, 10, 100, \dots, 10^5$. Then, for a fixed N , draw a *single image* of pure noise (the image x_T), and perform the backward process described in the previous section (Eq. 67), where the score s_t is estimated using $S_1(N)$ and $S_2(N)$. This yields 2 samples denoted $x_0^{(i,N)}$ to indicate that they are obtained by the two models $S_i(N)$.

Figure 33 shows a result of the experimentation. The questions that arise then are: does $x_0^{(i,N)}$ resemble closely or remotely an image from B_i ? does $x_0^{(1,N)}$ resemble $x_0^{(2,N)}$? The first question raises the issue of whether the obtained sample is possibly a mixture of images from the training database, or is it truly new. The second question concerns the uniqueness of the transformation process from the normal distribution to a hypothetical distribution p_0 .

As long as $N < O(10,000)$, $S_1(N)$ and $S_2(N)$ produce different images but ones that resemble an image from the database more closely as N decreases. For $N = 10,000$, the generated images $x_0^{(1,N)}$ and $x_0^{(2,N)}$ are different from the database. However, they are different from each other, which raises questions because it seems that two transformation processes are at work (recall x_T is the same noise image given to both backward processes). However, as soon as $N = 100,000$, the synthesized images $x_0^{(1,N)}$ and $x_0^{(2,N)}$ by $S_1(N)$ and $S_2(N)$ are not only different from the images closest to the two databases as before, but they are also very close to each other (red rectangle), indicating that a single process is indeed learned.

We are witnessing a transition from models that behave like large memories to models that effectively learn a probability distribution as long as the number of training images is sufficient. For 80×80 images, for a **U-Net** with $7.6 \cdot 10^6$ parameters, the transition seems to occur around $N \sim 10^5$, and it occurs around $N = O(10^4)$ for 40×40 images. However, it is not certain that a simple extrapolation of the training batch size would suffice for high-resolution images. That being said, one should not stop at the criterion of similarity between the generated sample and the closest sample from the training database to assess the quality of a generator.

³⁰This is the method of *score matching* (Hyvärinen, 2005).

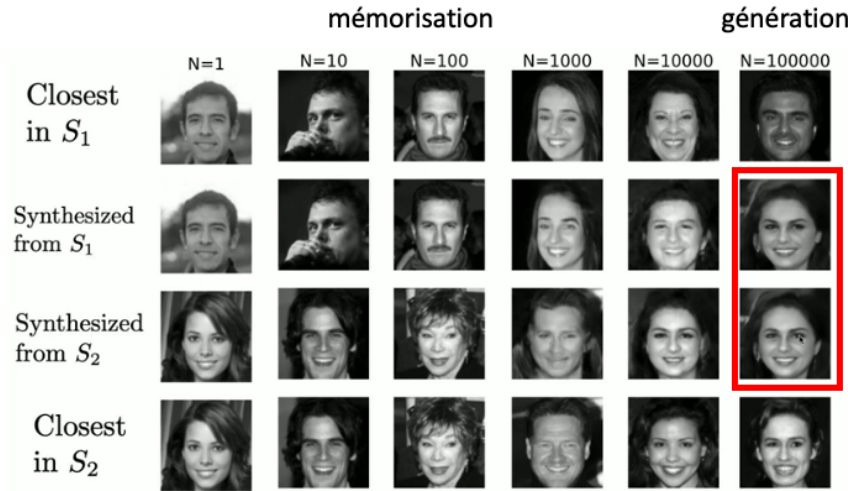


FIGURE 33. Two generative models S_1 and S_2 are trained with two non-overlapping databases, each of size N . Then, the same noise image is given to both models to synthesize a new image (80×80). The image from the database that best approximates this synthesized image can be found.

So, a properly trained denoising neural network indeed learns a distribution $p(x)$, whether it's for face photos, indoor photos, etc., for which it was not *a priori* imaginable that there would be such an underlying probability density. In high dimensions, there are phenomena of probability concentration on typical sets (Shannon, 1948; Jaynes, 1957), so it is possible that the description of the structures of this set in the case of photos is not as complex as it may seem *a priori*. Indeed, if U-Net networks manage to overcome the curse of dimensionality, it is because they have captured something, a form of regularity of the underlying distribution: "what is it?" that is the question.

4. SUMMARY

In this article, after briefly reviewing Fourier analysis and classical wavelet analysis, as well as studying the denoising of synthetic images with fixed regularity (C^α), we examined why, in the period from approximately 1995 to 2005, research focused on constructing orthonormal wavelet bases attempting to adapt to the signal's geometry. However, approximation errors in these bases did not reach the theoretical optimum. The advent of neural networks around the 2010s changed the landscape. For example, the use of deep networks such as DnCNN and U-Net (2015) is an example. On the other hand, the technique of generating samples from a density $p(x)$ by Score Diffusion has shed new light. The score $\nabla_x \log p(x)$, a concept developed by R. Fisher, can be directly learned by a network performing perfect denoising. This score, and thus this network, allows to invert a Markov process which, starting from a sample drawn from a simple d -dimensional normal distribution, produces a sample from $p(x)$. Studying the performance of such networks on C^α images shows that they achieve the desired optimum. The wavelet bases produced adapt perfectly to the geometry of the images. This property is preserved when applied to face photos, or even indoor photos. They are therefore more efficient than "traditional" methods. Moreover, by analyzing according to the size of the training samples, it has been shown that from a minimum size, the networks can learn an underlying probability density for natural images, as surprising as it may seem. These results open perspectives ranging from the field of research in mathematics to philosophical questions about the existence of universal underlying structures, through very practical considerations on the development of such models so that they are indeed able to generalize.

ACKNOWLEDGEMENTS

Zahra Kadkhodaie and Florentin Guth gave me access to their pre-trained U-Net models as well as the code for generating C^α images. With them and Gadriel Peyré, I was able to exchange ideas to develop this note. Nasser Eslahi gave me access to the CurveLab library (v2.1.3) and to his own ACT algorithm for using *curvelets*.

CODES

I used the MATLAB (The MathWorks, 2024) and Mathematica (Wolfram Research, Inc., 2022) environments. An implementation of the *wavelet steerable* library by Simoncelli and Freeman (1995) is available on the following github site: <https://github.com/TetsuyaOdaka/SteerablePyramid>. The BLS-GSM algorithm by Rajaei (2014) is available on the site <https://www.ipol.im/pub/art/2014/86/>.

REFERENCES

- Bruna, J., Mallat, S., 2013. Invariant scattering convolution networks. *IEEE Transactions on Pattern Analysis and Machine Intelligence* 35, 1872–1886. doi:10.1109/TPAMI.2012.230.
- Candes, E.J., Donoho, D.L., 2000. Curvelets, multiresolution representation, and scaling laws. *Proceedings of SPIE - The International Society for Optical Engineering* 4119. doi:10.1117/12.408568.
- Candès, E., Demanet, L., Donoho, D., Ying, L., 2006. Fast discrete curvelet transforms. *SIAM Journal on Multiscale Modeling and Simulation* 5. doi:10.1137/05064182X.
- Candès, E., Guo, F., 2002. New multiscale transforms, minimum total variation synthesis: Applications to edge-preserving image reconstruction. *Signal Processing* 82, 1519–1543. doi:10.1016/S0165-1684(02)00300-6.
- Chang, Z., Koulieris, G.A., Shum, H.P.H., 2023. On the design fundamentals of diffusion models: A survey [arXiv:2306.04542](https://arxiv.org/abs/2306.04542).
- Cheng, S., Morel, R., Allys, E., Ménard, B., Mallat, S., 2024. Scattering spectra models for physics. *PNAS Nexus* 3, pgae103. doi:10.1093/pnasnexus/pgae103.
- Cheng, S., Ting, Y.S., Ménard, B., Bruna, J., 2020. A new approach to observational cosmology using the scattering transform. *Monthly Notices of the Royal Astronomical Society* 499, 5902–5914. doi:10.1093/mnras/staa3165.
- Donoho, D.L., 2000. Orthonormal ridgelets and linear singularities. *SIAM Journal on Mathematical Analysis* 31, 1062–1099. doi:10.1137/S0036141098344403.
- Dossal, C.H., Le Pennec, E., Mallat, S., 2011. Bandlet Image Estimation with Model Selection. *Signal Processing* 91, 2743–2753. doi:10.1016/j.sigpro.2011.01.013.
- Eslahi, N., Aghagolzadeh, A., 2016. Compressive sensing image restoration using adaptive curvelet thresholding and nonlocal sparse regularization. *Trans. Img. Proc.* 25, 3126–3140. doi:10.1109/TIP.2016.2562563.
- Ferroukhi, M., Ouahabi, A., Attari, M., taleb ahmed, A., 2019. Medical video coding based on 2nd-generation wavelets: Performance evaluation. *Electronics* 8, 88. doi:10.3390/electronics8010088.
- Guth, F., Coste, S., De Bortoli, V., Mallat, S., 2022. Wavelet score-based generative modeling, in: Koyejo, S., Mohamed, S., Agarwal, A., Belgrave, D., Cho, K., Oh, A. (Eds.), *Advances in Neural Information Processing Systems*, Curran Associates, Inc.. pp. 478–491. [arXiv:2208.05003](https://arxiv.org/abs/2208.05003).
- Herbert, R., 1956. An empirical bayes approach to statistics, in: *Proceedings of the third berkeley symposium on mathematical statistics and probability*, pp. 157–163.
- Hergt, L., Amara, A., Brandenberger, R., Kacprzak, T., Réfrégier, A., 2017. Searching for cosmic strings in cmb anisotropy maps using wavelets and curvelets. *Journal of Cosmology and Astroparticle Physics* 2017, 004–004. doi:10.1088/1475-7516/2017/06/004.

- Hyvärinen, A., 2005. Estimation of non-normalized statistical models by score matching. *Journal of Machine Learning Research* 6, 695–709.
- Jaynes, E.T., 1957. Information theory and statistical mechanics. *Phys. Rev.* 106, 620–630. doi:10.1103/PhysRev.106.620.
- Kadkhodaie, Z., Guth, F., Simoncelli, E.P., Mallat, S., 2024. Generalization in diffusion models arises from geometry-adaptive harmonic representations, in: *The Twelfth International Conference on Learning Representations*. arXiv:2310.02557.
- Kingma, D.P., Welling, M., 2013. Auto-Encoding Variational Bayes. arXiv e-prints arXiv:1312.6114.
- Kong, Z., Deng, F., Zhuang, H., Yu, J., He, L., Yang, X., 2023. A comparison of image denoising methods. arXiv:2304.08990.
- Korostelev, A., Tsybakov, A., 1993. *Minimax Theory of Image Reconstruction*. Lecture notes in statistics, Springer-Verlag.
- Krizhevsky, A., Sutskever, I., Hinton, G.E., 2012. Imagenet classification with deep convolutional neural networks, in: Pereira, F., Burges, C., Bottou, L., Weinberger, K. (Eds.), *Advances in Neural Information Processing Systems*, Curran Associates, Inc.
- Le Pennec, E., Dossal, C., Peyré, G., Mallat, S., 2007. Débruitage géométrique d'image dans des bases orthonormées de bandelettes, in: *GRETSI 07*, Troyes.
- Le Pennec, E., Mallat, S., 2005a. Bandelet image approximation and compression. *Multiscale Modeling & Simulation* 4. doi:10.1137/040619454.
- Le Pennec, E., Mallat, S., 2005b. Sparse geometric image representations with bandelets. *IEEE transactions on image processing : a publication of the IEEE Signal Processing Society* 14, 423–38. doi:10.1109/TIP.2005.843753.
- Lee, G.R., Gommers, R., Waselewski, F., Wohlfahrt, K., O'Leary, A., 2019. Pywavelets: A python package for wavelet analysis. *Journal of Open Source Software* 4, 1237. doi:10.21105/joss.01237.
- Liu, Z., Luo, P., Wang, X., Tang, X., 2015. Deep learning face attributes in the wild, in: *Proceedings of International Conference on Computer Vision (ICCV)*.
- Mallat, S., 2008. *A Wavelet Tour of Signal Processing, Third Edition: The Sparse Way*. 3rd ed., Academic Press, Inc., USA.
- Mallat, S., Peyré, G., 2008. Orthogonal Bandlet Bases for Geometric Images Approximation. *Communications on Pure and Applied Mathematics* 61, 1173–1212. URL: <https://hal.science/hal-00359740>.
- Mallat, S., Peyré, G., 2007. A review of bandlet methods for geometrical image representation. *Numerical Algorithms* 44. doi:10.1007/s11075-007-9092-4.
- Mclaughlin, M., Grieggs, S., Ezekiel, S., Ferris, M., Blasch, E., Alford, M., Cornacchia, M., Bubalo, A., 2015. Bandelet denoising in image processing. doi:10.1109/NAECON.2015.7443035.
- Miyasawa, K., et al., 1961. An empirical bayes estimator of the mean of a normal population. *Bull. Inst. Internat. Statist* 38, 1–2.
- Rajaei, B., 2014. An Analysis and Improvement of the BLS-GSM Denoising Method. *Image Processing On Line* 4, 44–70. <https://doi.org/10.5201/ipo1.2014.86>.
- Rama Lakshmi, G., Divya, G., Bhavya, D., Sai Jahnavi, C., Akila, B., 2023. A review on image denoising algorithms for various applications, in: Bindhu, V., Tavares, J.M.R.S., Vuppapapati, C. (Eds.), *Proceedings of Fourth International Conference on Communication, Computing and Electronics Systems*, Springer Nature Singapore, Singapore. pp. 839–847.
- Raphan, M., Simoncelli, E.P., 2011. Least squares estimation without priors or supervision. *Neural Comput.* 23, 374–420. doi:10.1162/NECO_a_00076.
- Ronneberger, O., Fischer, P., Brox, T., 2015. U-net: Convolutional networks for biomedical image segmentation, in: Navab, N., Hornegger, J., Wells, W.M., Frangi, A.F. (Eds.), *Medical Image Computing and Computer-Assisted Intervention – MICCAI 2015*, Springer International Publishing, Cham. pp. 234–241.

- Shannon, C.E., 1948. A mathematical theory of communication. *The Bell System Technical Journal* 27, 379–423, 623–656.
- Simoncelli, E., Freeman, W., 1995. The steerable pyramid: A flexible architecture for multi-scale derivative computation, pp. 444 – 447 vol.3. doi:10.1109/ICIP.1995.537667.
- Song, Y., Sohl-Dickstein, J., Kingma, D.P., Kumar, A., Ermon, S., Poole, B., 2021. Score-based generative modeling through stochastic differential equations, in: *International Conference on Learning Representations*.
- Starck, J.L., Candes, E., Donoho, D., 2002. The curvelet transform for image denoising. *IEEE Transactions on Image Processing* 11, 670–684. doi:10.1109/TIP.2002.1014998.
- Starck, J. L., Donoho, D. L., Candès, E. J., 2003. Astronomical image representation by the curvelet transform. *A&A* 398, 785–800. doi:10.1051/0004-6361:20021571.
- Sze, V., hsin Chen, Y., Yang, T.J., Emer, J.S., 2017. Efficient processing of deep neural networks: A tutorial and survey. *Proceedings of the IEEE* 105, 2295–2329.
- Tang, Y., Salakhutdinov, R., Hinton, G., 2012. Robust boltzmann machines for recognition and denoising, pp. 2264–2271. doi:10.1109/CVPR.2012.6247936.
- The MathWorks, I., 2024. Matlab version: 24.1.0.2537033 (r2024a). URL: <https://www.mathworks.com>.
- Tweedie, M., 1947. Functions of a statistical variate with given means, with special reference to laplacian distributions, in: *Mathematical Proceedings of the Cambridge Philosophical Society*, Cambridge University Press. pp. 41–49.
- Uhlenbeck, G.E., Ornstein, L.S., 1930. On the theory of the brownian motion. *Phys. Rev.* 36, 823–841. doi:10.1103/PhysRev.36.823.
- Vergara, O., Ochoa, H., Sánchez, V., 2008. A comparison of the bandelet, wavelet and contourlet transforms for image denoising. *Mexican International Conference on Artificial Intelligence* 0, 207–212. doi:10.1109/MICAI.2008.63.
- Wang, H., Fan, L., Guo, Q., Zhang, C., 2020. A review of image denoising methods. *Communications in Information and Systems* 20, 461–480. doi:10.4310/CIS.2020.v20.n4.a4.
- Wiener, N., 1949. *Extrapolation, Interpolation, and Smoothing of Stationary Time Series: With Engineering Applications*. The MIT Press. doi:10.7551/mitpress/2946.001.0001.
- Woiselle, A., Starck, J.L., Fadili, J., 2010. 3d curvelet transforms and astronomical data restoration. *Applied and Computational Harmonic Analysis* 28, 171–188. doi:10.1016/j.acha.2009.12.003.
- Wolfram Research, Inc., 2022. *Mathematica* 13.1. URL: <https://www.wolfram.com>.
- Zarka, J., Guth, F., Mallat, S., 2021. Separation and Concentration in Deep Networks, in: *ICLR 2021 - 9th International Conference on Learning Representations, Vienna / Virtual, Austria*.
- Zarka, J., Thiry, L., Angles, T., Mallat, S., 2020. Deep network classification by scattering and homotopy dictionary learning, in: *International Conference on Learning Representations*.
- Zhang, J., Zhang, H., Shi, X., Geng, S., 2019. High noise astronomical image denoising via 2g-bandelet denoising compressed sensing. *Optik* 184, 377–388. doi:<https://doi.org/10.1016/j.ijleo.2019.04.029>.
- Zhang, K., Zuo, W., Chen, Y., Meng, D., Zhang, L., 2017. Beyond a Gaussian Denoiser: Residual Learning of Deep CNN for Image Denoising. *IEEE Transactions on Image Processing* 26, 3142–3155. doi:10.1109/TIP.2017.2662206.